Coupling Polar Adhesion with Traction, Spring, and Torque Forces Allows High-Speed Helical Migration of the Protozoan Parasite Toxoplasma

Georgios Pavlou, Bastien Touquet, Luis Vigetti, Patricia Renesto, Alexandre Bougdour, Delphine Débarre, Martial Balland, Isabelle Tardieux

ACSNANO

www.acsnano.org

ARTICLE

Coupling Polar Adhesion with Traction, Spring, and Torque Forces Allows High-Speed Helical Migration of the Protozoan Parasite *Toxoplasma*

Georgios Pavlou, Bastien Touquet, Luis Vigetti, Patricia Renesto, Alexandre Bougdour, Delphine Debarre, Martial Balland, and Isabelle Tardieux*

Cite This: https://dx.doi.org/10.1021/acsnano.0c01893

Read Online

ACCESS | Metrics & More | Article Recommendations | Supporting Information

ABSTRACT: Among the eukaryotic cells that navigate through fully developed metazoan tissues, protozoans from the Apicomplexa phylum have evolved motile developmental stages that move much faster than the fastest crawling cells owing to a peculiar substrate-dependent type of motility, known as gliding. Best-studied models are the *Plasmodium* sporozoite and the *Toxoplasma* tachyzoite polarized cells for which motility is vital to achieve their developmental programs in the metazoan hosts. The gliding machinery is shared between the two parasites and is largely characterized. Localized beneath the cell surface, it includes actin filaments, unconventional myosin motors housed within a multimember glideosome unit, and apically secreted transmembrane adhesins. In contrast, less is known about the force mechanisms powering cell movement. Pioneered biophysical studies on the sporozoite and phenotypic analysis of tachyzoite actin-related mutants have added complexity to the general view that force production for parasite forward movement directly results from the myosin-driven rearward motion of the actin-coupled adhesion sites. Here, we have interrogated how forces and substrate adhesion−de-adhesion cycles operate and coordinate to allow the typical left-handed helical gliding mode of the tachyzoite. By combining quantitative traction force and reflection interference microscopy with micropatterning and expansion microscopy, we unveil at the millisecond and nanometer scales the integration of a critical apical anchoring adhesion with specific traction and spring-like forces. We propose that the acto-myoA motor directs the traction force which allows transient energy storage by the microtubule cytoskeleton and therefore sets the thrust force required for *T. gondii* tachyzoite vital helical gliding capacity.

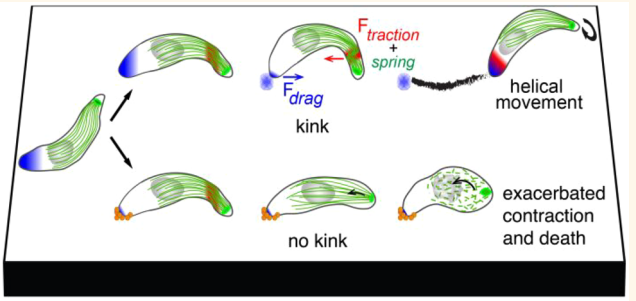

KEYWORDS: *cell migration, cell focal contact, 3D collagen, Toxoplasma, traction force microscopy, reflection interference contrast microscopy, expansion microscopy*

Across eukaryotic phyla, cell migration is an evolutionary conserved function which appears vital for both free living protozoans and metazoans.[1] In metazoans, cells such as fibroblasts and leukocytes use a wide spectrum of adhesion-dependent motility modes conjointly defined as crawling and primarily driven by the dynamics of the cell actin−myosin cytoskeleton.[2,3] These cells crawl with the help of dynamic actin-powered membrane protrusions that fold at the leading edge as a flat lamellipodium or as a variety of pseudopodia-like membrane projections. Firmly attached to the substrate upon coordinated assembly of integrin-driven adhesive platforms, the lamellipodium is a hallmark of the mesenchymal cell migration mode in 2D and 3D micro-environments. These anchoring multimolecular platforms allow the development of actomyosin bundles that tune contractile forces between the front and trailing margins and eventually lead to the release of trailing adhesions, hence allowing cell forward translocation.[4,5] Likewise, metazoan cells—as well as large free-living protozoans—can display a

Received: March 4, 2020
Accepted: May 20, 2020
Published: May 20, 2020

https://dx.doi.org/10.1021/acsnano.0c01893
ACS Nano XXXX, XXX, XXX−XXX

more versatile motility mode and cope with heterogeneous 3D microenvironments. In addition to the lamellipodium style, they can adopt diversified pseudopodia mechanisms that, combined with a range of relative cell-matrix adhesion and actomyosin contractility, account for the rapid amoeboid type of motility (~10 to 20 μm/min *versus* less than 1 μm/min for the lamellipodia mode).[6] Alternatively, fibroblasts can utilize an amoeboid−mesenchymal hybrid type of 3D migration called lopobodial during which a pressure-driven bleb-like membrane protrusion stems at the leading margin from the piston-like forward movement of the nucleus itself driven by the cortical actomyosin contractility.[7] Biophysical studies have proved instrumental in mapping and measuring the development of forces in cells, and they brought insights on how cells differentially regulate the adhesion−contractile balance to spatiotemporally control the adhesion assembly deassembly cycle and achieve productive forward movement in different contexts.[8]

Intriguingly, unicellular eukaryotic parasites from the ancient phylum of Apicomplexa have evolved an adhesion- and actin-dependent motility mode that differs from the mesenchymal, amoeboid, lobopodial repertoire and enables the microbes to glide within host tissues and across barriers to follow their complex stepwise developmental program. The several thousand members of the Apicomplexa phylum include among the world's most pre-eminent mammal-invasive protozoan parasites. In humans, *Plasmodium* spp. are inoculated in the vascularized dermis extracellular matrix (ECM) by a blood-feeding mosquito which hosts parasites in salivary glands. *Plasmodium* displays a prolonged asexual developmental phase in red blood cells, which results in a range of clinical outcomes known as malaria, impacting human populations in tropical and subtropical regions of the Earth. Its relative *Toxoplasma gondii* is present in a large assortment of endotherm metazoans worldwide. Being ingested with contaminated food and water, *T. gondii* is hosted quasi-silently by possibly up to a third of the human population in tissues such as the brain, retina, and heart and skeletal muscles. However, in case of immune dysfunction, *T. gondii* can re-emerge from these tissues and proliferate, causing life-threatening or debilitating complications.[9]

Throughout their life cycle in their respective hosts, both *Plasmodium* and *T. gondii* ensure their perpetuation by undergoing multiple cell differentiation events that give rise to specific developmental stages with sizes of several microns, harboring a crescent shape and endowed with high motility skills.[10] Best studied are the *Plasmodium* slender mature sporozoite inoculated in the host skin and the *T. gondii* bulky highly replicative tachyzoite stages that glide 10 times faster than the amoeboid cells without folding any of the crawling-associated protrusions.[10−12] Instead, they share a robust longitudinal apico-basal polarity which persists during the generally unidirectional motile activity with the apex leading.[13] Whereas the *Plasmodium* sporozoite moves on a circular path in either counterclockwise (CCW) or clockwise (CW) directions with an irregular stop and go kinetics,[13] it can also occasionally adopt a random motion or a corkscrew-like pattern *in vivo*.[14,15] Instead a left-handed helix characterizes the path the mosquito-restricted ookinete *Plasmodium* stage used to move in Matrigel-based 3D matrices.[16] The *Toxoplasma* tachyzoite can similarly glide CCW on a circular path under 2D *in vitro* settings but often uses a CCW helical trajectory or a succession of the two mechanisms over the same gliding sequence.[11,17] Another intermittent 2D movement termed twirling accounts for the stationary CW rotation executed by the upright-positioned tachyzoite around its posterior end.[18] The corkscrew-like mode of gliding, which is the obligate mechanism in 3D reconstituted or *in vivo* environments was proposed to relate to the 2D helical mode of gliding.[19] The latter typically starts with a CW short motion, follows with a 180° twist; meanwhile, the body flattens on the substrate before twisting up and flipping on the side, which allows starting another helical cycle.[11,18]

To initiate and sustain all types of gliding activity, both the sporozoite and tachyzoite rely on the regulated secretion of adhesive protein oligomers at the cell surface[20,21] that, once delivered at the apical tip, can coengage with ECM proteins and short cortical actin filaments organized beneath the plasma membrane. Force production driving parasite movement has long been considered to directly translate from the apico-basal translocation of the ECM-bound adhesins coupled to the flowing actin filaments and their enzymatic-mediated release of these adhesins at the trailing edge.[22,23] It is the Apicomplexa specific, fast, nonprocessive, single-headed motor myosin A (MyoA) that was assigned an essential powering role in pulling backward the apically initiated actin filaments and the captured adhesins.[24,25] Upstream from MyoA however, the *T. gondii* tachyzoite additionally requires myosin H (MyoH) to propel actin filaments from the parasite apical tip formed by the conoid,[26] a retractile appendage missing in *Plasmodium*. Both MyoA and MyoH molecules function within a multisubunit complex identified as glideosome[22] that also comprises several regulatory subunits and scaffolding partners.[27−29] Specifically for MyoA, the glideosome associated proteins (GAPs) anchor the motor machinery to the plasma membrane and the lining internal bilayered membrane complex (IMC) which underside is tethered to a cytoplasmic array of cortical microtubules (cMTs), the number and arrangement of which typify each Apicomplexa species and developmental stage.[27,30]

However, the recent introduction of force microscopy, reflection interference contrast microscopy (RICM) and optical tweezers in conjunction with molecular genetics in the *Plasmodium* field has added more complexity to the prevalent force production model.[31] A key observation is the discrepancy between the speed of the retrograde flow of optically trapped microbeads on the apical surface of the sporozoite and the speed achieved during typical circular gliding, the former being up to 50% faster than the latter.[31] In addition, several distinct areas of contact between the moving sporozoite and the substrate were uncovered at the apex, base, and center over the circular path and were shown to display specific on−off dynamics,[13] whereas the genetic loss of a surface-exposed adhesin reported to function during motility was found to trigger a speed increase in the retrograde flow and a concomitant decrease in force production.[31] Collectively, these studies bring compelling evidence for the assembly of distinct force-generating adhesive structures which differentially control production of the force required for migration.

By contrast, how forces and dynamic adhesions coordinate in space and time and integrate with the impressive high-speed helical path that features the *T. gondii* tachyzoite gliding mechanism has been much less investigated. Intriguingly, the rearward capping of nanobeads bound to the tachyzoite surface was shown not to require an intact actomyosin system but rather a polarized secretory−endocytic cycle that would locally drive membrane tension.[32] On the other hand, qualitative

https://dx.doi.org/10.1021/acsnano.0c01893
ACS Nano XXXX, XXX, XXX−XXX

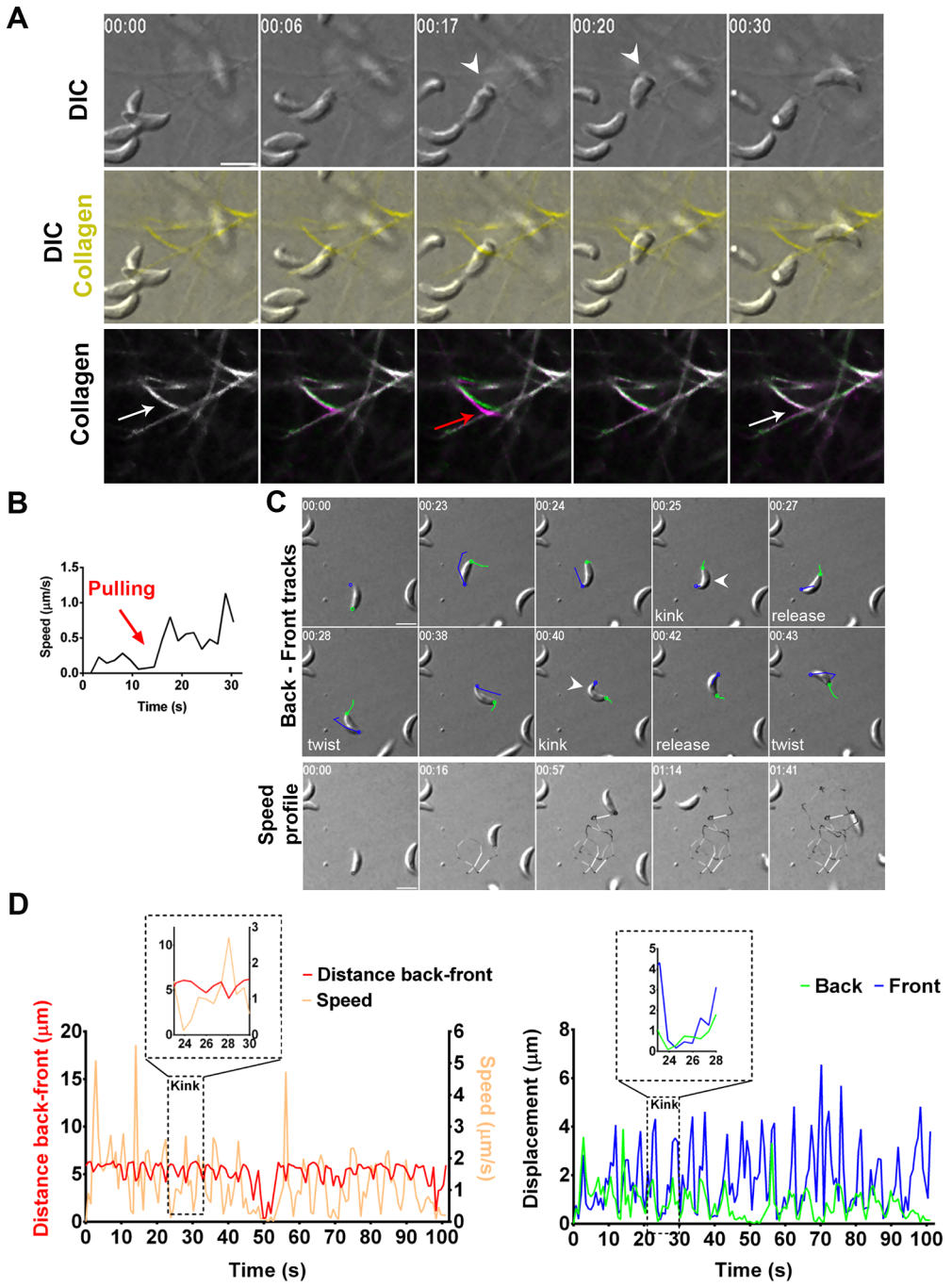

Figure 1. Tachyzoite pulls on the collagen fibers prior to helical acceleration. (A) Successive images from a time lapse of a tachyzoite navigating within a 3D-meshwork of rat collagen1 fibers prelabeled with the CNA35-GFP collagen chimeric probe. Panels show images of (top) DIC, (middle) DIC-GFP over, giving yellow-colored fibers, (bottom) the fiber initial (t_0, green) and over time (t_x, magenta) positions when encountered by the moving tachyzoite. The overimposition of the green and magenta signals comes as white (white arrows) when the fiber maintains the t_0 position, whereas the separation between the green (t_0) and magenta (t_x) signals attests two distinct positions overtime. The backward displacement indicates the parasite pulls on the fiber (red arrow), whereas the graph (B) documents that this pulling coincides with the parasite low speed. Next the acceleration step coincides with the merge back of the green and magenta signals that signs for the release of fiber tension post motion. (C) Successive DIC images from a time lapse of a tachyzoite undergoing helical gliding on fibronectin-coated glass. (Top) back (green) and front (blue) tracks over three last frames (t_{x-2} to t_x) are shown, (bottom) speed profile is shown from black to white scaling with increasing speeds. All white arrowheads point to the kink, all scale bars: 5 μm, time is in minutes/seconds. (D) Graph (left) plots the tachyzoite back−front distance (red line) and the speed based on the back tracking (light orange); note that the value close to zero corresponds to the time the tachyzoite twirls, hence the apex is out of focus and the back-front distance not measurable (right) the *xy* displacement for both the back (green) and front (blue) sites over the helical sequence. Zoomed of a typical kink step for both graphs shown as inlays.

RICM allowed identifying an early tachyzoite contact with the substrate at the cell front and its rearward translocation which was assumed to directly power the force-producing parasite movement.[33] In this study, we revisited the mechanisms

https://dx.doi.org/10.1021/acsnano.0c01893
ACS Nano XXXX, XXX, XXX−XXX

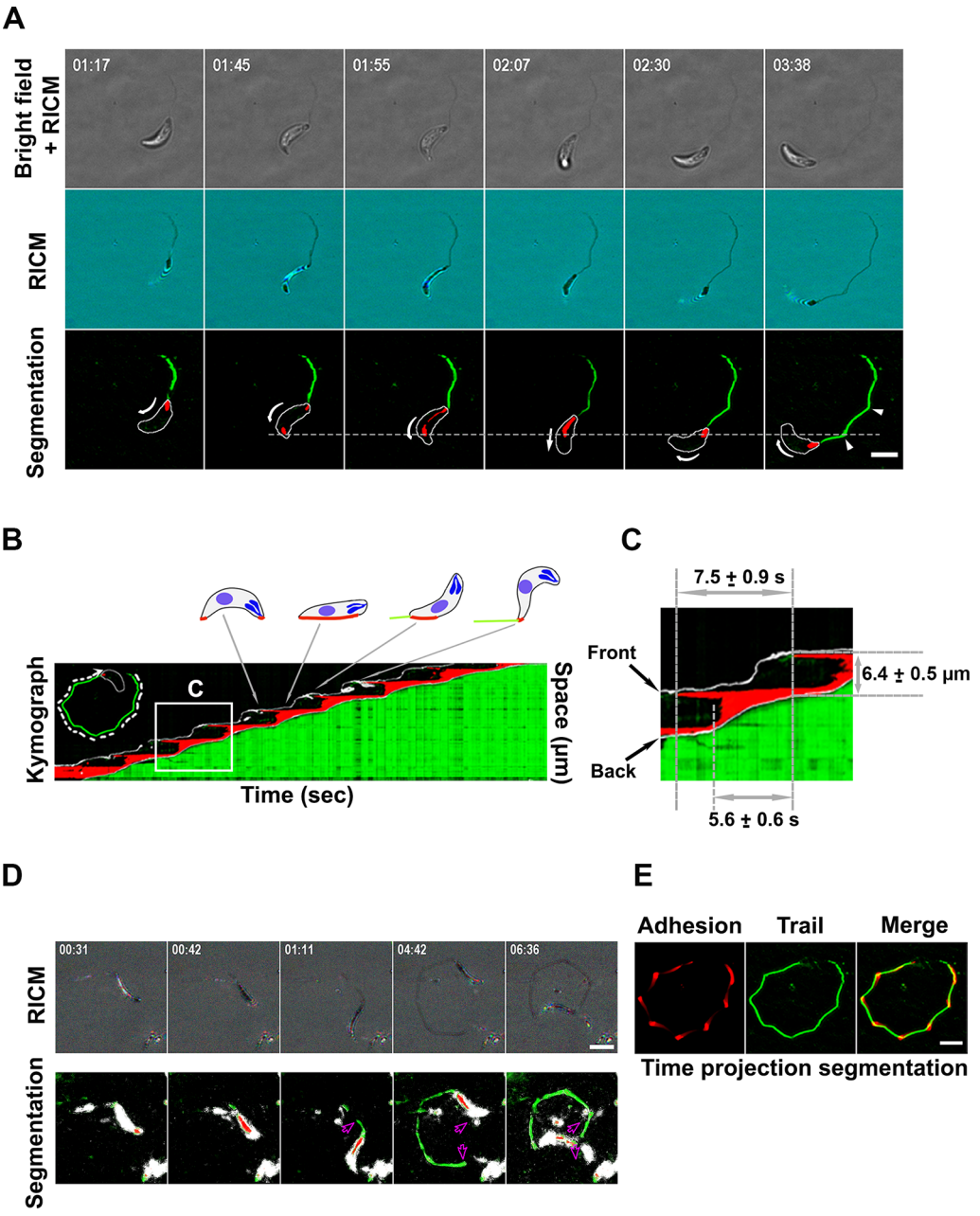

Figure 2. Helical cycle starts with an apical site of adhesion that constraints sliding of both the parasite and the parasite posteriorly shed trail. (A) Successive RICM images from a time lapse of a tachyzoite undergoing helical motion on a glass coverslip. Panels show (top) simultaneous bright-field (BF) and RICM images, (middle) blue and green RICM images superimposed and displayed as RGB, (bottom) segmentation of BF and RICM images showing the parasite outline (white), areas of close contact between the glass and the moving parasite (red), and material shed behind as trail (green). White arrows indicate the direction of the parasite movement. The dotted line marks the position of the initial contact over one helical cycle and delineates the trajectory angular point. (B,C) Kymograph of the whole gliding sequence from (A) and for a single zoomed helical cycle (C) shows the evolution of the close contact area along the trajectory over time. (D) Successive three-color RICM images (shown as RGB) from a time lapse of a tachyzoite undergoing helical motion on a poly-L-lysine-coated glass coverslip (top) and corresponding segmentation with the Weka FIJI plugin (bottom). The pink arrows indicate that over time the tachyzoite pulls on the trail that slides without breaking but follows the polygonal trajectory imposed by the initial anchoring sites. (E) Time projection of the segmented close contact areas over the gliding sequence on which (left) the longest-lived attachment points are brightest, (middle) the trails are green, and (right) adhesion and trails are overimposed. Note that angles in the polygonal path coincide with both the long-lived close contacts and the kinks. All scale bars: 5 μm; time is in minutes/seconds.

underpinning the helical gliding of *T. gondii* by combining quantitative live imaging with traction force microscopy, quantitative RICM, micropatterning and expansion microscopy. We provided evidence for a spatiotemporal coordination of an actoMyoA-based traction force produced at a stable apical adhesion site and a spring-like force which, driven by the left-handed cMT spiral orientation, directs straightening and helical propelling of the *T. gondii* tachyzoite.

RESULTS/DISCUSSION

Tachyzoite Pulls on the Collagen Fibers in a 3D Meshwork Prior to Accelerating with a Helical Motion.

https://dx.doi.org/10.1021/acsnano.0c01893
ACS Nano XXXX, XXX, XXX−XXX

Pioneering work on *T. gondii* 3D *in vitro* motility has relied on Matrigel-based matrices under rather elastic and homogeneous conditions.[19] However, *in vivo*, most ECM microenvironments are enriched in a nonlinear, anisotropic, and dynamic fibril-rich meshwork. Because collagens are dominant ECM components that form multiscale fibrils withstanding tensile forces,[34] we analyzed how the *T. gondii* tachyzoite moves within a confined collagen fibril-based matrix. Whereas the tachyzoite squeezed its body to pass through the meshwork, it first paused and bent, showing an apical deviation as it next accelerated, possibly with a rotation around its main axis, to escape from the collagen fibrils (Figure 1A,B and Supporting Information Figure S1, Movie 1, and Movie 2). Using a fluorescent probe selectively associated with collagen fibrils,[35] we applied a temporal color-code (green and magenta) and identified fibers encountered by the motile tachyzoite that shifted backward before returning to initial position as the parasite propelled forward (Figure 1A, Supporting Information Movie 1). This fiber backward displacement was seen in all cases of moving tachyzoites encountering a fiber (n = 10), and qualitatively indicated that the parasite exerted pulling forces on the surrounding fibers.

To get more mechanistic insights on the front-rear spatiotemporal coordination over the helical gliding cycle, we further analyzed the changes in the tachyzoite shape with high spatiotemporal acuity using a 2D setting. We observed a yet undefined apical inward bending immediately post the initial clockwise arc motion and concomitant with the parasite pause (Figure 1C). Indeed, tracking the front and back revealed a shortening of the parasite that coincided with an apical flexure and thus an increased curvature, resembling the observation made within the fibrous 3D matrix, and which we defined as the kink step. Associating with the apical pole arrest we detected the contraction of the cell body and retraction of the posterior pole. Next the apex re-extended and lifted up, a phase defined as the kink release, while the tachyzoite straightened and slid to further twisted in the typical CCW motion (Figure 1C, Supporting Information Movie 3a and Movie 3b, slow motion). Accordingly, not only the instantaneous speed was about null during the kink step and reached maximal value as the latter relaxed back (Figure 1D), resulting in the characteristic periodic speed fluctuations documented under 3D conditions.[19] No such pattern was detected when the parasite performed the 2D-restricted CCW circular trajectory (Supporting Information Figure S1B,C and Movie 4). Of note, high temporal resolution live imaging of *Plasmodium* sporozoites also reveals alternating periods of rapid movement in which they travel up to one body length and periods of slow movement in which they more firmly adhere to the substrate, thereby indicating that distinct adhesion types operate during motility.[13] Although such kinetics was associated with the sporozoite body stretching upon firm adhesion of its polar and center regions to the substrate and the subsequent thrust in speed,[13] no peculiar apical deformation that could resemble a kink has been observed to initiate movement. We proposed that the kink deformation and the subsequent body extension might reflect the tension built in the tachyzoite cytoskeleton to achieve the thrust force required for the helical twisting motion.

Apical Focal Adhesion Behaves as a Firm Long-Lived Anchor That Constrains Sliding of the Parasite Body. Because the apical kink suggests the assembly of a specific contact between the parasite front and the substrate, which would be appropriate for building up tension in the *T. gondii* cytoskeleton, we first used qRICM to monitor the parasite-substrate distance. In contrast to a recent study,[33] we used high-speed (30 frames/s), multicolor RICM with simultaneous transmitted-light imaging coupled with machine-learning-based image processing to achieve a precise segmentation of close contact regions between the parasite and the substrate at high temporal resolution (33 ms) over thousands of frames (Figure 2 and Supporting Information Movie 5 and Movie 6). In addition to the low-distance patches detected between the parasite basal pole and the substrate even in absence of movement, we found that at the onset of a helical cycle, the membrane of the tachyzoite apex came in contact with the glass surface. Because these RICM-detected signals coexisted with motion, we assumed they accounted for two polar parasite−substrate adhesive areas in agreement with Tosetti and collaborators[33] and similarly to what was found for the *Plasmodium* sporozoite.[13] Crucially, the apical contact remained static over the full length of the helical cycle (7.5 ± 0.9 s), and the posterior contact progressively expanded to account for ∼80% of the tachyzoite length along its major axis (Figure 2A−C, see kymographs, Supporting Information Movie 5). Upon release of the kink, the parasite propelled forward and shifted orientation before it started a new front attachment. For each helical cycle, the kink step could be *a posteriori* inferred through the mix of parasite-derived membrane hydrophobic droplets and surface-exposed proteins/glycoproteins left as a complex trail behind the cell edge onto the substrate, a common feature of Apicomplexa motile stages (Figure 2A,D,E).[11,36] Quantitative modeling of the RICM signal provides transverse dimensions for these trails of ∼70 nm (isotropic) or 100 nm (width) and 40−60 nm (height). By comonitoring the parasite helical motion and the trail assembly in real time, we were able to uncover that the tachyzoite not only slid on the adhesive tracks it built itself but could also pull these, an observation that has not been reported for the RICM data collected on *Plasmodium*.[13] These observations suggest a continuous nature of the shed material that remained close but not firmly fixed on the substrate (Figure 2D and Supporting Information Movie 6), which would agree with membrane components including lipids as previously deduced from the analysis of fixed samples.[11] Importantly, the sliding trajectories of the shed material once pulled by the moving tachyzoite appeared constraint by the periodically distributed firm anchors, which could occasionally be stripped off from the substrate (Supporting Information Movie 6). In further support of these periodic stable anchors, the time projection of the trail trajectory postimage segmentation allowed positioning the longest-lived parasite−substrate contacts at each angular point of the trajectory, matching the initial apical anchoring sites (Figure 2E). The relative homogeneity in the trail observed at our RICM resolution cannot inform on a specific distribution or arrangement in proteins and lipids upon specific secretory events or/and due to local physical constraints that would compose the periodic anchors. The microneme-stored MIC2 is seen as the adhesion prototype that bridges the parasite motor system and ECM ligands during motility. Indeed partial or full silencing of the *mic2* expression significantly impairs both the helical and twirling motions.[37,38] This double default argues more for a MIC2 contribution to the posterior adhesion force,[37] hence *mic2* KO parasites show a reduced capacity to bind to host cells and collagen-coated surfaces.[38] Consistently,

https://dx.doi.org/10.1021/acsnano.0c01893
ACS Nano XXXX, XXX, XXX−XXX

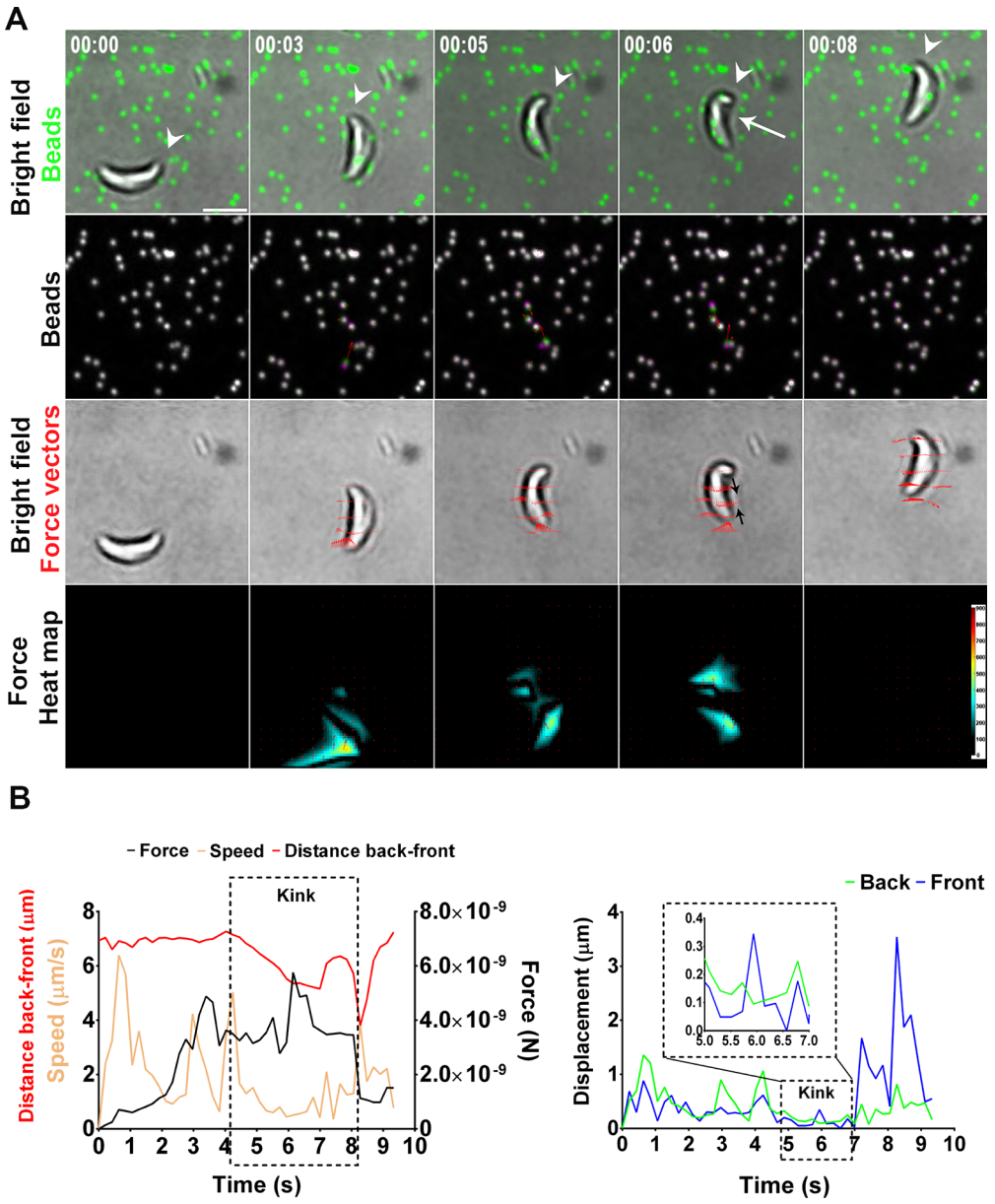

Figure 3. Helical motion includes the development of apical traction at the kink site and basal dragging forces. (A) Traction force microscopy (TFM) images were taken at the time a parasite glides on a 2 kPa PAA gel in which fluorescent TFM beads are embedded underneath the gel surface itself coated with fibronectin (20 μg/mL). Panels show (top) bright-field (BF) and TFM beads composite images; white arrowheads indicate the apex of the tachyzoite, and white arrow marks the kink, (second row) beads alone, (third row) BF with force vectors computed by the MATLAB TFM code. Red arrows indicate the force direction and value; black arrows have been manually added to ease visualization of the two longitudinal forces and their orientation, (bottom) force heat map computed MATLAB TFM code. Scale bar: 5 μm, time is in minutes/seconds; au for force heat map. (B) (Left) Speed (light orange line), the back to front body distance (red line) and the traction force applied by the parasite over time (black line) are shown with a zoomed inlay (black dotted line) at the kink step time, and (right) the back and front displacement (green and blue trajectories, respectively) are shown with a zoomed inlay (black dotted line) at the kink time.

when the *T. gondii* tachyzoite expresses only residual levels of the rhomboid protease (ROM4) in charge of cleaving the surface-exposed MIC2, MIC2 molecules accumulate at the surface of the parasite that can no longer glide forward but instead shows enhanced twirling motility.[39] Similarly, when *Plasmodium berghei* sporozoites express a mutant version of the MIC2 homologue TRAP that cannot be processed by the rhomboid protease, the parasite can no longer disengage its posterior pole from the substrate and move forward.[36] Whereas we detected both SAG1 and MIC2 proteins in patches over successive segments of the helical trails postfixation and immunolabeling, we did not find MIC2-specific enrichment at the angular adhesion regions that were accurately identified using the RICM live sequences as recognition pattern (Supporting Information Figure S2). Therefore, it is possible that another unknown adhesin(s), which would not integrate the retrograde flow, might modulate force production at the parasite apex in line with the turnover-specific adhesion sites built by the *Plasmodium* sporozoite during circular gliding.[13] In addition, monitoring the apico-basal flow of optically trapped beads pinned out that specific adhesions do not integrate the apico-basal capping process, yet

https://dx.doi.org/10.1021/acsnano.0c01893
ACS Nano XXXX, XXX, XXX−XXX

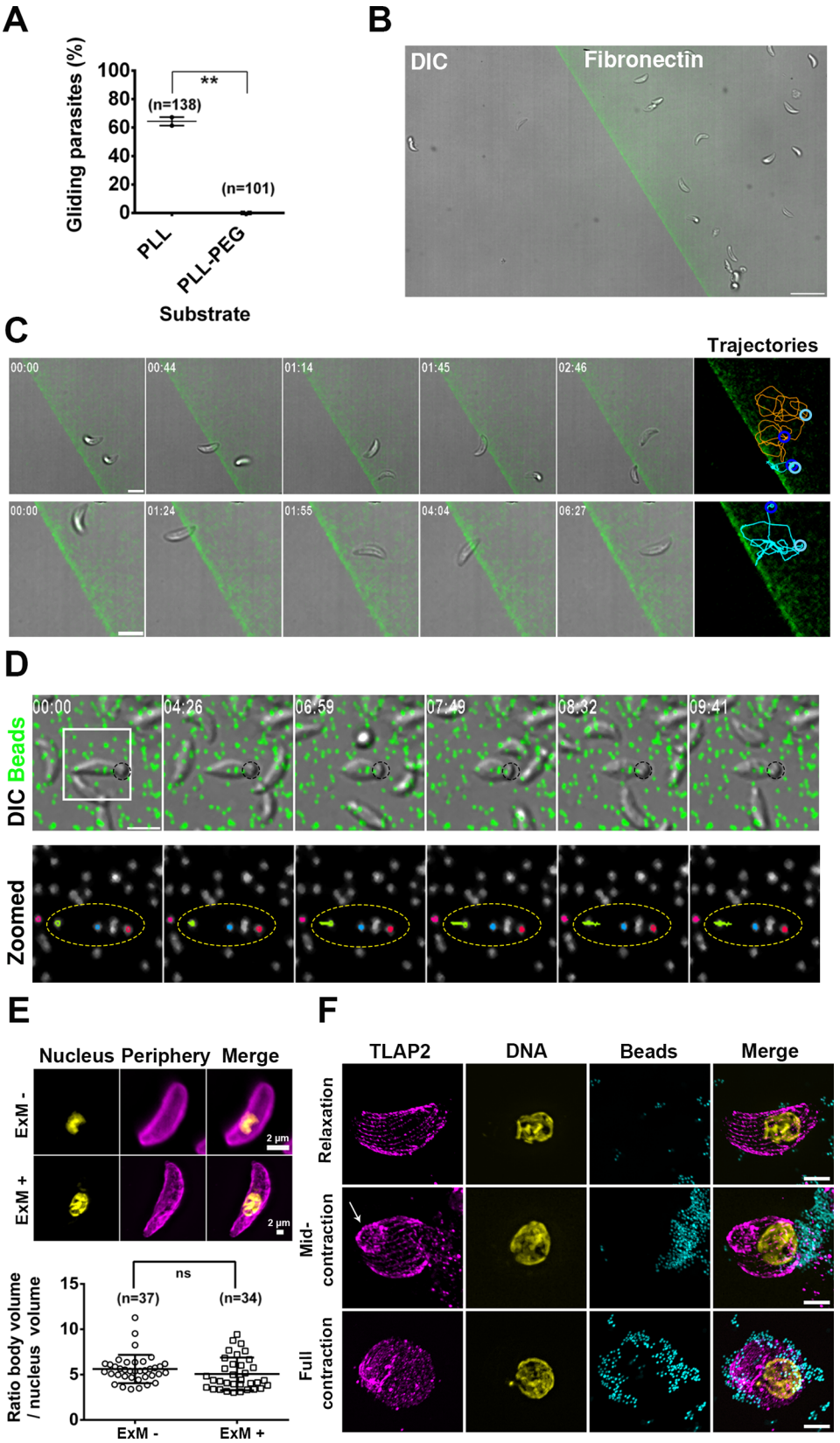

Figure 4. Front adhesion to and back disengagement from the substrate are both required for kink formation and traction force development. (A) Percentage of tachyzoites that moved by at least one body length displacement over a 20 min period post contact with poly-L-lysine (PLL) or poly(ethylene glycol) (PEG) chains grafted on PLL coating, unpaired *t* test, $^{**}p = 0.021$. (B) Large view of the poly-L-lysine PEG−fibronectin composite micropattern shows that tachyzoites are selectively retained in the fibronectin area, which is fluorescently labeled by fibrinogen-Alexa647, scale bar: 15 μm. (C) Images from a sequence of two (top) or one (bottom) representative gliding tachyzoite(s) that fail to pass over the fibronectin−PLL−PEG demarcation line being incapable of interacting apically with PEG. Instead they elicit twirling around their posterior end bound to fibronectin and regain helical motion once apically sensing fibronectin. Blue and

https://dx.doi.org/10.1021/acsnano.0c01893
ACS Nano XXXX, XXX, XXX−XXX

Figure 4. continued

cyan circles in the trajectories window indicate the initial and the final position of the tachyzoite over the several-minute gliding sequence. Trajectories were reconstituted by tracking the tachyzoite base, which unlike the apex stays in focus even during twisting and twirling motions. (D) TFM on a tachyzoite posteriorly immobilized on fibronectin through carboxylated microbeads (black circle). (Top) Selective inward displacement of TFM beads (green) beneath the apex of the immobilized parasite occurs during sustained contraction, whereas the beads relax back to initial position upon parasite relaxation, (bottom) zoomed white square from top, showing the colored trajectories; note the large yellow trajectory that attests significant bead inward displacement, the yellow dotted ellipsoid delineates the tachyzoite. (E) Confocal images showing a representative tachyzoite immunolabeled for the GAP45 protein (pink) that delineates the parasite periphery and PI stained for DNA (yellow) prior ExM (ExM−) and after ExM (ExM+), maximal projection intensity are presented, compare the scale bars that attests the physical magnification of the ExM specifmen. The graph shows the ratio of the body and nucleus volumes after 3D reconstruction prior (ExM−) and after ExM (ExM+), Kruskal−Wallis test, NS, p = 0,17. (F) ExM on tachyzoites posteriorly immobilized on beads (cyan) and immunolabeled for the cortical MT-associated TLAP2 protein (pink) and PI stained for DNA (yellow), (top) no contraction has yet started, (middle) contraction has started, note the apical humpy deformation in the cMT cytoskeleton indicated with a white arrow, (bottom) cMT disruption at a latest time of tachyzoite sustained contraction. Scale bars: 5 μm unless indicated, time is in minutes/seconds. The ExM allowed reaching about a 70 nM xy resolution thanks to a ∼3−5-fold increase in the biological sample size.

they can optimize force production. Accordingly, the trap-like protein (TLP) was proposed to promote firmer adhesion to the substrate by enabling specific actin remodeling underneath the plasma membrane. Such function would explain why TLP causes specific slowdown of the actin-dependent flow.[31] With these in mind, we next interrogated whether the firm stable apical anchor formed by the moving tachyzoite and localized at the kink could indeed serve as a platform for force transmission by using traction force microscopy (TFM). These assays also allowed testing whether the kink-induced cell shortening could be associated with tension stored in the parasite that would be released to promote the thrust required for productive helical movement.

Traction force Spatiotemporally Associates with the Kink and Coincides with Body Dragging. To design the TFM assay, we first identified a substrate in which the stiffness was sufficient to allow helical gliding while being elastic enough to measure substrate deformations *via* a displacement field analysis performed using fluorescent beads embedded into the polyacrylamide (PAA) hydrogel. Particle image velocity (PIV) combined with single-particle tracking allowed analyzing substrate deformation with a spatial resolution in the range of tenth of nanometers. Tracking in space and time the tachyzoite posterior pole and scoring as motile those that performed at least one body length displacement, we found that stiffer substrates such as glass (n = 73) and 40 kPa PAA (n = 55) correlated with optimal gliding skills, whereas lowering stiffness gradually decreased the frequency and duration of the motile behavior. Yet, the tachyzoites retained a short-lasting ability to perform helical motion on the soft 2 kPa PAA substrate (n = 103) (Supporting Information Figure S3). Applying TFM[40] to parasites gliding on 2 kPa fibronectin−PAA substrate, we obtained a traction vector map and identified an early inward-oriented traction force stemming at the cell front and exerted longitudinally in line with the backward displacement of the in-gel beads (*i.e.*, TFM beads) underneath the apical part of the parasite (Figure 3A and Supporting Information Movie 7a and Movie 7b, slow motion). As the force progressively increased, concomitant dragging of the parasite body occurred and accounted for the TFM bead's displacement underneath the posterior pole in the direction of the parasite motion, in line with the previous detection of trails being pulled by the tachyzoite (Supporting Information Movie 6). Relaxation of the TFM beads back to their initial position was recorded immediately after the kink release and the parasite forward acceleration (Figure 3A,B). Pioneering TFM on the *Plasmodium* sporozoite has allowed uncovering two longitudinal forces applied at each pole during circular gliding, alike what we found for the *T. gondii* tachyzoite undergoing helical gliding. A large force localized at the posterior adhesion site peaked just prior sporozoite de-adhesion, whereas a lower pulling traction force at the apex pointed toward the center. In contrast to what we detected for the tachyzoite, large forces were also found to point orthogonally toward the sporozoite center,[13] where they promote body stretching and thus favor close contact of the whole cell with the substrate—an obligate requirement for circular gliding—without contributing to force production.[41] Therefore, although both the tachyzoite and sporozoite likely use a stalling force at the back, which upon rupture of the adhesive contact contributes to a thrust force, the spatiotemporal distribution and intensity of the forces during their specific gliding cycle (*i.e.*, helical *versus* circular) likely differ. Accordingly, the overall force during the helical cycle was computed to a few nanoNewtons (∼1 to 4 nN, n = 10) with an increment over the kink step, therefore significantly higher than the 100−200 pN range inferred for cortical forces using laser trap on nongliding *T. gondii* tachyzoites[42] or gliding *Plasmodium* sporozoites.[31] By comparison, the nanoNewton range characterize forces applied by both bacteria and mammalian cells on their surroundings.[43]

***Toxoplasma* Apical Focal Adhesion Is Essential to Switch from Nonproductive Twirling to Productive Helical Motion.** To demonstrate the functional contribution of the apical body adhesion to the subsequent helical gliding, we sought interfering with the parasite adhesive step at the apical traction force site. First, we screened for substrates not permissive to parasite adhesion using several chemicals of distinct charge and wettability properties. We found that tachyzoites were unable to stabilize and glide on the densely packed polymeric poly(ethylene glycol) (PEG) brushes grafted on poly-L-lysine (PLL) (Figure 4A) similarly to what was reported for *Plasmodium* sporozoites.[44] Therefore, composite substrate was photopatterned: the parasites underwent energetic gliding on the fibronectin-coated area when approaching the demarcation line between the fibronectin and PLL−PEG-juxtaposed areas. The tachyzoites stopped when facing PEG, sometimes sliding on it prior to stepping back in a reverse motion while still posteriorly bound to fibronectin (Figure 4B,C and Supporting Information Movie 8 and Movie 9). They responded to the exclusive basal attachment by spinning around the main axis in a typical twirling nonproductive motion[18] until the front region was eventually caught again in an interaction with fibronectin,

https://dx.doi.org/10.1021/acsnano.0c01893
ACS Nano XXXX, XXX, XXX−XXX

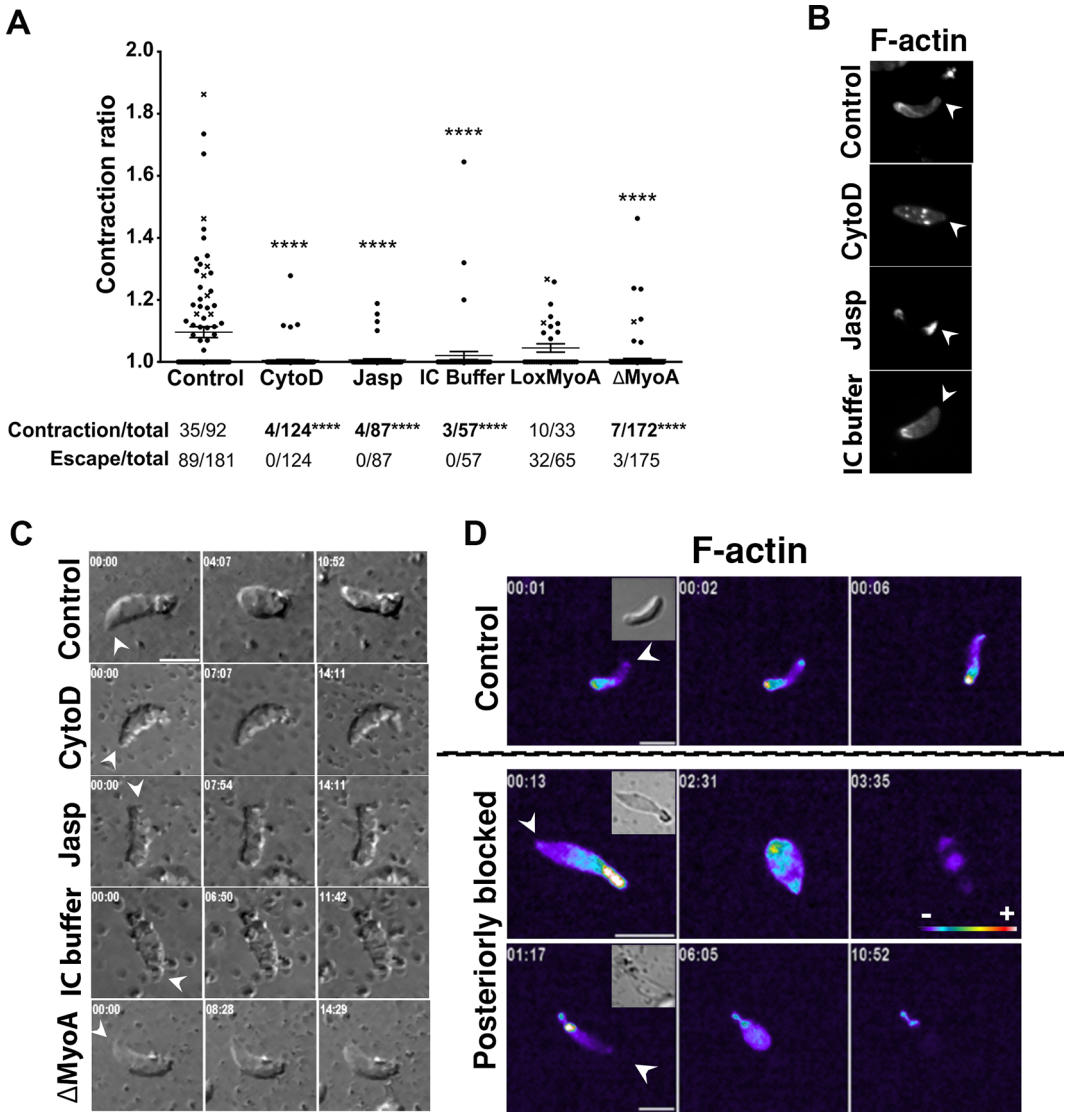

Figure 5. Prolonged and exacerbated tachyzoite contraction relies on intact actin filaments and MyoA motor. (A) Graph shows the contraction ratio after posterior immobilization on beads over a 20 min period for (i) wild-type control tachyzoites expressing the F-actin chromobody-Emerald (Acb-E) and incubated in EC buffer supplemented or not with 1 μM cytochalasin D or 1 μM jasplakinolide actin poisons or in IC buffer, and (ii) for tachyzoites before (LoxMyoA) and after (ΔMyoA) Cre-mediated excision of the *myoA* gene. Kruskal–Wallis test, ****p < 0.001 Dunn's multiple comparisons with the control genotype. Table below the graph shows (i) proportions of number of parasites contracted over the total and (ii) proportions of number of parasites that escape over the total. For both, chi square test, ****p < 0.001 Fisher's exact test with the control. (B) Confocal images of tachyzoites showing F-actin prior to record the contractile behavior. Maximal projection intensities are presented. (C) Representative DIC images of tachyzoites posteriorly immobilized to monitor both contractile behavior and bead-capping ability under each setting over a 20 min period (57 > n > 181 depending on the actin poison used and 65 > n > 165 for *myoA* KO, 3 independent assays). (D) Representative fluorescent images of F-actin dynamics in tachyzoites expressing the Ach-E undergoing helical gliding (top panel) or sustained contraction upon posterior immobilization (middle and bottom panels); DIC images are presented as inlays for each sample. Heat map intensity is presented in arbitrary units.

hence restoring the tachyzoite ability to perform helical trajectory. These data reinforce the view that the tachyzoite builds an apical stable adhesion site with the substrate that is compatible with the development of traction force. As we showed that both adhesion and force spatiotemporally coincide with the kink-like deformation, we expected then that the thrust productive force would be at least partly driven by the relaxation of the kink, which drives the slight lift of the parasite apex. Of note, this thrust force might also require some contribution from the parasite basal contact which loosens when traction operates allowing both dragging and retraction of the body. Given that tachyzoites must overcome the resistance of the 3D—nonlinear—meshwork to navigate in physiological microenvironments, the acceleration induced upon the kink release should provide the right thrust to pass through the meshwork of fibers they pulled on. Accordingly, we next addressed how the contact and dragging force at the cell back identified by, respectively, RICM and TFM contribute to the helical gliding mode of the tachyzoite.

Adhesion–De-adhesion Coupling at Both Poles Drives the *Toxoplasma* Apical Kink and Its Release, in Turn Promoting the Helical Thrust Force. We designed another TFM assay in which the tachyzoite would be unable to disengage its posterior pole from the substrate using submicron

https://dx.doi.org/10.1021/acsnano.0c01893
ACS Nano XXXX, XXX, XXX–XXX

sticky beads. As already reported in the context of membrane flow or cortical forces studies,[32,42] the beads deposited on the tachyzoite surface underwent apico-basal translocation. However, because in our setting the bead's surface engaged covalent interactions not only with the parasite but also with the fibronectin layer in a configuration that forced the former to stay posteriorly immobilized on the latter, the cell forward progression could be hindered (Figure 4D). Such posteriorly constraint tachyzoites never formed the apical kink (n = 0/92) and, instead, underwent a directional, minute time scale and repetitive inward-oriented contraction visualized by the whole body rounding (Figure 4D and Supporting Information Movie 10). The TFM captured the displacement of in-gel beads suitably positioned underneath the apex of the immobilized parasite consistent with a sustained apical traction force, and therefore a sustained adhesion between the parasite front and the substrate (Figure 4D, zoomed panel, yellow bead and trajectory). The prolonged force application induced pronounced shrinkage of the cell body along the longitudinal axis and eventually led to membrane damages to the extent the tachyzoite was likely wounded beyond repair. Meanwhile, we observed that the in-gel beads shifted back to almost the initial position, which we assumed to relate to the sudden relaxation of the cell "ghost" when internal tension fell (Figure 4D and Supporting Information Movie 10). Strong evidence for the rupture of the plasma membrane upon excessive contraction of the YFP-expressing tachyzoite was provided by the acute loss of fluorescence that occurred immediately after maximal cell rounding and concomitantly with the relaxation of the cell (Supporting Information Figure S4). The relaxed tachyzoite cell looked mis-shapen for the rest of the recording time as expected for a cell ghost, therefore attesting that the exacerbated and sustained contraction induced cell death. To next visualize the deleterious effect of the long-lasting contraction on internal cytoskeletal structures at the nanoscale resolution, we applied the expansion microscopy technique (ExM)[45] and first validated the isotropic expansion of the specimen with the 3D co-reconstruction of the tachyzoite body and nucleus prior and after expansion (Figure 4E). We then analyzed a tachyzoite line engineered to express a fluorescent version of TLAP2, a protein aligned with the 22 cMTs,[30] and confirmed that during the prolonged contraction period, the capped beads accumulated posteriorly while the spiral cMTs deformed. We first observed an apical hump in the cMT network (Figure 4F, middle panel), and eventually, the latter fell apart while the capped beads were redistributed over the damaged surface (Figure 4F, bottom panel). Overall, these data support that the kink rose from the interplay between the apical adhesion/base de-adhesion and the forces generated at both poles rather than from the apical traction force only. They also highlight that creating unbalance between the front and back responses can result in a contractile force that imposes a mechanical compression to the cMT network to which it cannot resist. The need for a balanced myosin-A-based contractile activity that stems at the tachyzoite apex and promotes disengagement of the posterior pole can explain why the genetically myosinA-deficient tachyzoites, which retain only residual motility, do not any longer undergo helical gliding.[37,32]

Tachyzoite Apico-Basal Contraction Requires Intact Actin Filaments and Myosin A Motor and Correlates Only Partially with the Requirements for Rearward Membrane Flow. Apart from the prolonged contraction and fatal outcome described earlier, we also observed that the tachyzoites, which were posteriorly immobilized, could either rotate on the beads, slightly contract, and move forward, hence those escaped (Supporting Information Movie 11) or remain inactive, hence those showed no contraction and stayed attached. To verify whether actin dynamics and MyoA motor the function of which are required for motility[25,46] would also contribute to the apically driven exacerbated contraction, we first defined a quantitative readout for measuring the contraction extend over time. Using the ratio between the resting body length (*i.e.*, no contraction) and the minimal body length (*i.e.*, maximum contraction) as a contraction indicator, we found that nearly half of the wild-type (WT) control parasites were able to escape from the immobilization setting, therefore attesting to the energetically active status of the specimens under study. Approximately 40% of the second half (n = 35/92) contracted over a wide range of amplitude, whereas 20% of this contracting population actually showed signs of irreversible damages (n = 7/35) (Figure 5A). Blocking actin dynamics with cytochalasin D (0.5 and 1 μM) or jasplakinolide (1 μM) that work through different mechanisms[47,48] almost abolished both the escape (*i.e.*, motile) and contractile behaviors. Of note, the few (less than 5%) tachyzoites that displayed contraction never reached the stage of high and sustained body compression, hence none of them died (Figure 5A). We confirmed the cytochalasin and jasplakinolide potency on tachyzoite actin as parasites expressing the fluorescent chromobody actin-Emerald (Acb-E)[49] displayed the typical drug-induced redistribution of actin filaments as, respectively, cytoplasmic aggregates and apical acrosome-like.[50] With the same readout, we also compared the contractile behavior of parasites following or not *MyoA* gene silencing using the well-characterized DiCre Lox MyoA strains.[24] We observed that loss of MyoA ($\Delta MyoA$) significantly altered the contractile capability of tachyzoites immobilized on their base when compared to the MyoA-expressing parental line (LoxMyoA) (ΔMyoA = 175, $p < 0.001$) (Figure 5A). Finally, we checked if the contractile activity was specific for tachyzoites metabolically ready for initiating motility by measuring the contraction of WT control tachyzoites kept in the Endo buffer which mimics the intracellular buffer (herafter referred to as IC buffer) and is known to drastically decrease microneme secretion (*i.e.*, adhesin delivery on the tachyzoite surface) and consequently motility.[20] Those tachyzoites showed the typical actin posterior network of intracellular tachyzoites[51] and were significantly inefficient at contracting under the posterior microbead setting (nIC = 57, $p < 0.001$ (Figure 5A–C and Supporting Information Movie 12). Finally, we monitored actin filaments in real time in Acb-E-expressing tachyzoites undergoing either helical gliding or forced contraction during the immobilization phase. The F-actin apical focus detected at the onset of the helical cycle remained discrete and rapidly resolved into the large stable basal F-actin pool, as reported[33,51] and in line with our force mapping assays. In contrast, an increasing F-actin signal was detected within the whole body, in particular, in the cell front upon prolonged contraction of the immobilized and rounding tachyzoites (Figure 5D and Supporting Information Movie 13). Eventually, the F-actin signal vanished, which fits with the loss of fluorescence observed with YFP-expressing tachyzoite artificially immobilized on the substrate through their basal pole (Supporting Information Figure S4), thereby confirming that the membrane had ruptured upon excessive

https://dx.doi.org/10.1021/acsnano.0c01893
ACS Nano XXXX, XXX, XXX−XXX

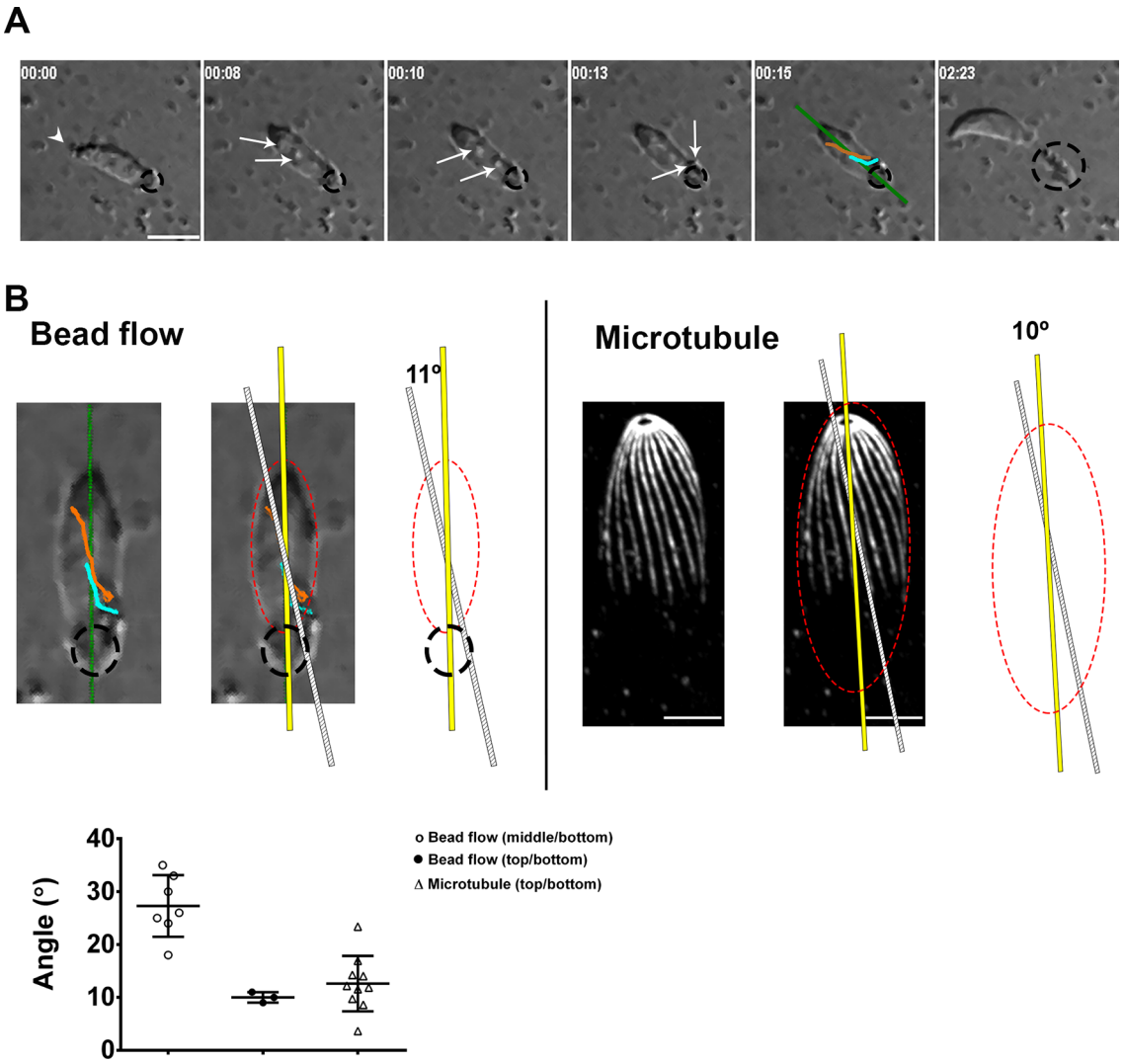

Figure 6. Apico-basal translocation of surface-bound microbeads follows a helical path that approximates the spiral direction of the tachyzoite cMTs. (A) Representative images of apico-basal bead capping monitored in real time for tachyzoites posteriorly immobilized on beads encircled with the dotted black line. The two surface-bound beads are indicated with white arrows, and their trajectory depicted in orange and cyan lines is shown on the fifth panel, before active escape of the tachyzoite from the immobilizing setting. In all panels, white arrowheads mark the tachyzoite apex; all scale bars: 5 μm, time is in minutes/seconds. (B) Zoomed panels show images and schematics for (left) trajectory of two beads over the capping time taken from the sequence shown in A, which deviates from the body main axis (yellow line) of about a 11° angle, while (right) the spiral cMTs visualized on an extracellular tachyzoite treated for U-ExM and stained with antipolyglutamylated tubulin show about a 10° angle orientation. (Bottom) Plot of the different angles calculated for the cMTs; the mean with SD is shown for each group (n = 10 tachyzoites, mean of 4 cMTs per tachyzoite) and for the capping bead flow (n = 9 tachyzoites). Please note the larger variability shown by the bead angles, which depends on the bead position at the initial time of capture and tracking.

contractile activity, leaving a tachyzoite ghost, the apex of which no longer attached to the substrate.

As the retrograde membrane flow process has been shown to operate in *T. gondii* tachyzoites in absence of the actomyosin system,[32] we analyzed how this process would operate for tachyzoites artificially immobilized on their base. Unlike previously,[32] we monitored in real time the bead-capping process and found that the loss of contractility driven by actin poisons and IC conditions did correlate with the inhibition of the rearward bead capping along the parasite surface ($57 > n > 181$ depending on the condition) (Figure 5C and Figure 6A and Supporting Information Movie 14), thus recapitulating the phenotype of formin 1(FRM1)-deficient tachyzoites[33] and consistent with the need of apically initiated actin filaments. However, on loss of myosinA,[46] whereas the tachyzoites showed almost no ability to contract (Figure 5A), they intriguingly maintained a bead-capping activity almost as efficient as tachyzoites from the parental line ($65 > n > 165$) (Figure 5C and Supporting Information Movie 12), in agreement with a MyoA contribution to force transmission rather than production.[32] Furthermore, along with these bead-translocation assays we observed in WT tachyzoites that the bead-capping process could precede productive helical movement (Figure 6A and Supporting Information Movie 14), and that the bead apico-basal motion could follow the cMT helical trajectory. To confirm this observation, we applied ExM with a recently refined near-native expansion microscopy (U-ExM) protocol,[52] and labeled the α,β-tubulin dimer that forms the cMT polymers taking advantage of the polyglutamylation post-translational modification of these isoforms.[53] With this level of resolution, we could measure the angle with the longitudinal axis made by the cMTs when they emanate at the apical polar

https://dx.doi.org/10.1021/acsnano.0c01893
ACS Nano XXXX, XXX, XXX−XXX

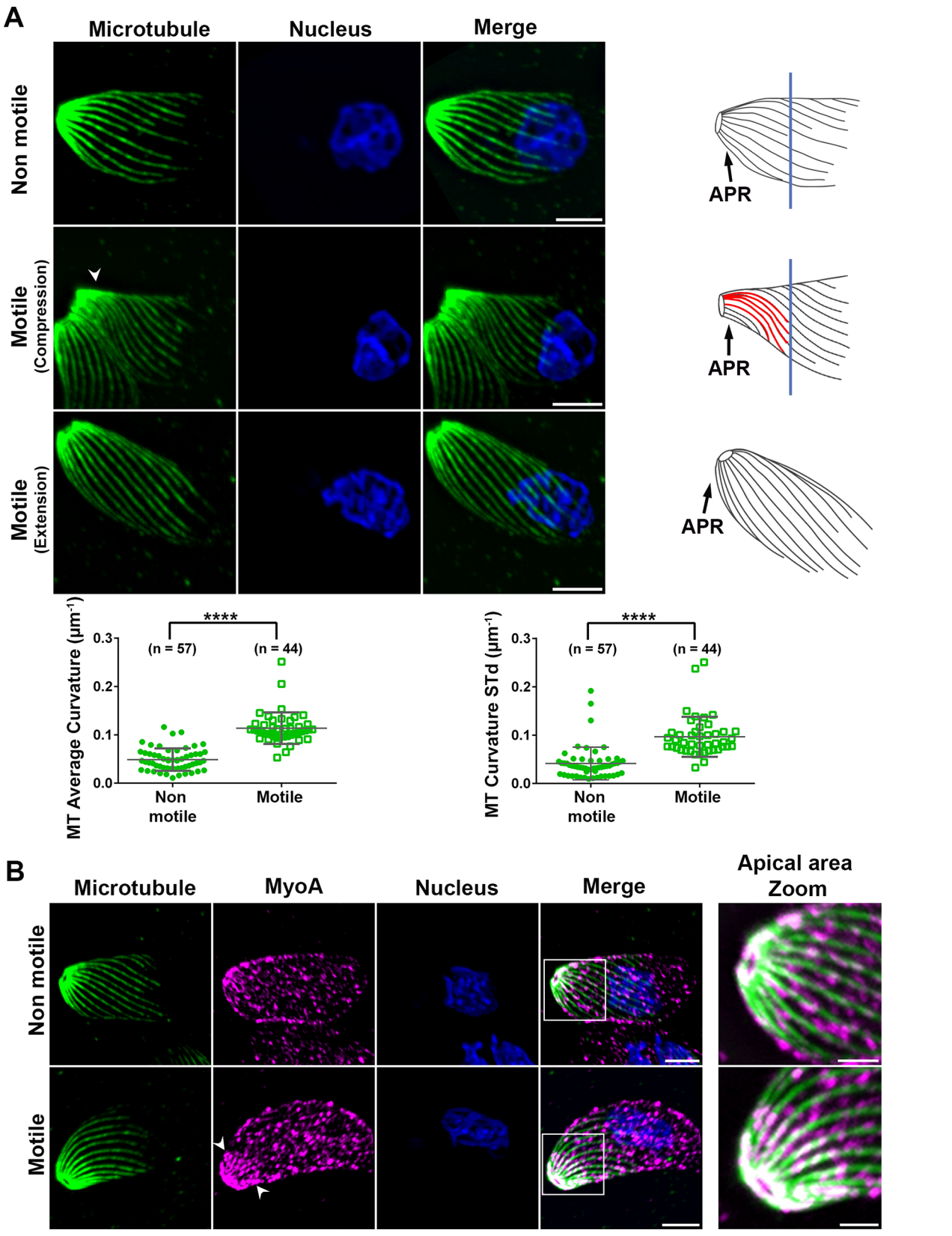

Figure 7. Curvature of cortical microtubules changes during helical gliding suggesting a spring-like mechanism apically driven by myosin-based contractile forces. (A,B) Confocal images representative of extracellular tachyzoites following U-ExM and immunofluorescence co-staining of (A) tachyzoite cMTs using antipolyglutamylated tubulin antibodies (green) and nucleus (blue). Maximal projection intensities of the cMTs from the tachyzoite ventral side are shown for (top) a nonmotile tachyzoite, (middle and bottom) two motile tachyzoites. Note the pronounced torsion and compression (white arrowhead, middle panel) and the extension (white arrowhead, bottom panel) that likely account for the spring like force underlying helical gliding. Right: Schematics of the cMTs for each stage show the highly curved cMTs at the apical region of the motile tachyzoites, drawn in red. (Bottom) Graph on the left shows a significant increase in mean curvature of the cMTs

https://dx.doi.org/10.1021/acsnano.0c01893
ACS Nano XXXX, XXX, XXX−XXX

Figure 7. continued

for the motile tachyzoites in torsion, unpaired *t* test, ***$p < 0.0001$ $n = 44$, when compared to the nonmotile ($n = 57$); graph on the right shows enhanced curvature amplitude over the length of single cMT for motile tachyzoites during the compression step ($n = 47$) when compared to nonmotile ($n = 57$) tachyzoites, unpaired *t* test, ***$p < 0.0001$. (B) Co-staining of the cMTs (green) and MyoA-HA tagged using anti-HA antibodies (purple) and the nucleus (blue). (Top) Nonmotile tachyzoite, (bottom) motile tachyzoite are shown. Note the clear MyoA signal enrichment at the apex of the motile parasite indicated with white arrowheads, which co-aligns with the MT signal. The right frames show zoomed areas delineated in the merge frames with a white square. All scale bars: 5 μm except for the B zoomed frames: 2 μm. The U-ExM protocol gave a 3−5-fold increase of the tachyzoite size and provided a ∼70 nM *xy* resolution. APR: Apical polar ring.

ring while approximating the angle made by the microbeads monitored over the capping process (Figure 6B and Supporting Information Movie 14). Although we observed for some beads that the angles were off the range of those made by the well-resolved cMTs, it is worth noting that these gaps mainly correspond to situations where the microbeads were tracked while they had already reached the minor axis plane of the ellipsoid tachyzoite. While traveling toward the posterior pole, the beads approached an area devoid of cMTs and often collided with the substrate before reaching the posterior pole, an observation already reported when monitoring the apico-basal trajectory of 0.6 μm beads delivered by laser trap to the surface of resting (*i.e.*, nonmotile) tachyzoites.[42] Collectively, these data indicate that the actomyosin system mobilized during the rearward bead translocation process has aligned with the longitudinal cMT network, this independently of the apical adhesion and thus before the apical traction force operates.

Curvature of Cortical Microtubules Significantly Changes during Helical Gliding, Suggesting a Spring-like Mechanism Apically Driven by Myosin-Based Contractile Forces. Triggered upon relaxation of the apical kink, the extension of the tachyzoite body coincided with the thrust force while the parasite rotated with an orientation dictated by the MTs' helical architecture (Figure 1C and Figure 3A and Supporting Information Movie 3a). In metazoans, the general ability of MTs to bear compressive loads imposed by contractile forces translates into a coordinated bending of MTs and to drive a spring-like force mechanism as exemplified with the rhythmically contracting cardiac myocytes.[54] To interrogate whether the cMTs could transiently store energy upon actomyosin activation and acts as a torsional spring to promote the required thrust for helical propelling, we analyzed the behavior of cMTs during helical motion. Whereas the U-ExM allows nanoscale resolution, it does not permit to affirm that the tachyzoites under observation were actually caught in motion. As under pro-gliding conditions, the tachyzoites displayed a statistically significant elongation of the nucleus as compared to the samples of either extracellular tachyzoites left in IC buffer or tachyzoites which had just invaded host cells ($n > 75$ for each condition, Supporting Information Figure S5A), we used the nucleus sphericity as first criterion. We next selected for tachyzoites associated with helical trails using the surface-exposed glycoprotein SAG1 known as robust trail marker,[11] which also bore an elongated nucleus ($p < 0.0001$, $n = 12$ motile helical and $n = 15$ intracellular) (Supporting Information Figure S5B). To analyze whether individual cMTs could display a specific compression, relaxation and torsion behavior in motile tachyzoites, we applied U-ExM and used both antiacetylated α-tubulin and antipolyglutamylated a,β-tubulin antibodies which have been widely used for labeling *T. gondii* cMTs.[53] When quantifying the curvature of the cMTs in nonmotile extracellular (Figure 7A, top panel) or nonmotile intracellular (Supporting Information Figure S5C, top panel) and motile parasites (Figure 7A, middle panel; Supporting Information Figure S5C, bottom panel), we observed for the motile specimens, a highly significant increase in the mean curvature of the MTs as compared to the nonmotile ones (Figure 7A, polyglutamylated tubulin, $p < 0{,}0001$, $n = 57$ nonmotile and $n = 44$ motile parasites) (Supporting Information Figure S5B,C, acetylated tubulin, $p < 0{,}0001$, $n = 24$ nonmotile and $n = 22$ motile tachyzoites). Importantly, the curvature amplitude over the length of a single MT was also significantly enhanced in gliding when compared to intracellular parasites as assessed by the standard deviation values of the curvature profile over the full length MTs (Figure 7A, polyglutamylated tubulin, $p < 0{,}0001$, Supporting Information Figure S5B,C, acetylated tubulin, $p < 0{,}0001$). The decreased interdistance between single cMT nearby the apical ring (APR) from where they emanate together with the observed nonuniform bending over the cMT length strongly argue for a specific compression occurring at the tachyzoite apex during cell movement. In addition, situations where the cMTs straightened at the apical region likely corresponded to the time of the thrust force occurring upon kink release (Figure 7A, bottom panel; see also schematics on the right). To further test the hypothesis of cooperation between the actoMyoA-based and the cMT-based cytoskeletons could contribute to force production at the kink, we performed U-ExM imaging of MyoA and cMTs simultaneously on either motile or nonmotile tachyzoites. To this end, we used a tachyzoite line that expresses a chimeric MyoA-HA protein under the endogenous promoter and anti-HA antibodies. A clear co-alignment of the MyoA and the cMTs was detected in the apical region of motile tachyzoites together with a local enrichment in MyoA when compared to nonmotile parasites (Figure 7B). Although it is not possible to ascertain that this situation reflects the kink step, the alignment between the MyoA and the cMTs makes plausible an indirect connection and thus argue for an energy transfer between the two cytoskeletons. In addition, this co-alignment is consistent with the helical path taken by the beads undergoing actin-based rearward capping. In metazoans cells, it was found that the MTs were embedded in a viscoelastic material provided by the surrounding medium and MT-associated proteins—in particular, kinesin motors[55]—that influence the MT ability to buckle and bear energy load.[54] Therefore, it would be worth investigating whether some MT or/and IMC protein partners - including the APR-associated kinesin,[56] proteins that coat the cMT length and alveolins— positioned at the apical flexure site could behave as pro-elastic elements and thus optimize a cMT driven spring-like reaction. Of note the intrinsic stable left-handed curvature of ≪resting≫ cMTs already sign for their ability to withstand large forces within the cytoplasm in agreement with their contribution to shape maintenance.[30,57] As the activation of

https://dx.doi.org/10.1021/acsnano.0c01893
ACS Nano XXXX, XXX, XXX−XXX

the actomyosin system translates into force-powering motility, it is plausible that the significant local increase in cMT curvature of motile tachyzoites accounts for higher compressive loads on the cMTs in response to the increased contractility. Indeed, when the tachyzoite underwent exacerbated actomyosin-driven contraction (Figure 4F) in a failed attempt to disengage its base from the adhesion site, the cMT cytoskeleton overcame its bending capacity and eventually broke up.

CONCLUSIONS

In this study, by combining surface sensitive biophysical techniques with high resolution-high speed 2D and 3D live imaging and expansion microscopy, we provided insights on how the *T. gondii* parasite couples cycles of adhesion−de-adhesion to the substrate with traction and spring-like force generation to achieve helical gliding, a function which is required for perpetuating *T. gondii* populations in the homeothermic hosts. Owing to its persistent structural polarity over the intracellular/extracellular cycles, the tachyzoite bypasses the canonical symmetry break most eukaryotic cells must undergo to start migrating.[58] In addition, although lacking the typical actomyosin II motor commonly used to generate traction in eukaryotes, *Toxoplasma* has evolved an Apicomplexa-restricted unconventional myosinA motor that, immobilized within the glideosome unit and between the membrane layers forming the pellicle at the cell surface, works on noncanonical actin filaments to activate motility.[29] The pellicle and the subtending twisted 22 microtubules provide the tachyzoite with a peculiar crescent shape and flexibility, which has proposed to act as the primary driver of the helical motion. We now demonstrate that the *T. gondii* tachyzoite must engage its apical region in a specific stable adhesion with the substrate that is compatible with the development of a balanced traction force and drives, in turn, the loosening of the posterior contact point, allowing retraction of the parasite base and dragging force. Therefore, similarly to what was found for the *Plasmodium* motile sporozoite, real time analysis of adhesion dynamics and force mapping supported by recently refined high spatiotemporal resolution imaging approaches and biophysics characterization applied to the *Toxoplasma* motile tachyzoite have challenged the classic model of Apicomplexa gliding motility. In addition to the backward capping of adhesion proteins at the cell surface, both parasite rely on a distinct class of adhesive contact that do not enter the rearward flow but directly contribute to build tension in the parasite cytoskeleton and produce force by strengthening anchors points with a specific on−off dynamics, hence regulating the motile process. Although these studies confirm the need to shift paradigm for a comprehensive mechanistic understanding of Apicomplexa gliding motility, they raised key questions on the nanoscale architecture of the singular adhesive platforms including the adhesin ligand identities on the extracellular side, the actin filament organization on the cytoplasmic side, but also how they would transmit tensional forces from the cytoskeleton to the ECM with the yet to clarify contribution of the MyoA motor, and eventually, it would be worth investigating their putative contribution for mechanotransduction. Providing indication of a spatiotemporally regulated cooperation between the tachyzoite actomyoA-based contractile activity and the helical flexible cMT ability to build tension, this study gives credit to pioneered kinematic analysis.[18] These results also highlight the necessity to delve deeper into the compressive, torsional, and tensile strengths of *Toxoplasma* tachyzoite and also *Plasmodium* sporozoite cMTs as some differences between the two stages could in part account for their specific motile behavior.

METHODS/EXPERIMENTAL

Parasite Strain Maintenance and Preparation for All Motility Live Assays. All media and products used for cell culture were from Gibco-Life Technologies (St Aubin, France) unless specified. *T. gondii* strains were propagated on *Mycoplasma*-free human foreskin fibroblast monolayers (HFFs) and grown in Dulbecco's modified Eagle medium (DMEM) supplemented with glutamax, 10% heat-inactivated fetal calf serum (FCS), penicillin (100 U/mL), and streptomycin (100 μg/mL) at 37 °C and 5% CO_2. The laboratory type 1 RH strain was used as well as the YFP-expressing RH[17] and the mutant deleted for the KU80 protein[59] (gift from V. Carruthers, Michigan University, USA; see Molecular Cloning section). The RH Δku80: DiCre/lox MyoA, RH Δku80: DiCre/ΔMyoA,[60] and the RH cbactinEmFP[49] expressing strains were given by M. Meissner (MLU Munich University, Germany) and hereafter designated LoxMyoA, ΔMyoA, or Ach-E, respectively. For most motility assays, tachyzoites were collected within a few hours following spontaneous egress from the HFF monolayers, and ∼10^5 cells were centrifuged in $HBSS^{++}$ supplemented with 0.2% FCS (0.2% HBSS). The pellet containing parasites was resuspended in 150 μL of 1% FCS HBSS (1% HBSS) and adjusted at 1.6 mM of $CaCl_2$ (1% HBSS-Ca^{2+}). Typically, when using the 18 mm diameter glass coverslip fitting chamber, 50 μL of the tachyzoite suspension was added to 100 μL of 1% FCS HBSS-Ca^{2+} covering the coverslip. The amounts of FCS, $CaCl_2$, and pharmacological reagents were adjusted upon need as described in each appropriate section.

Molecular Cloning. A mCherry (mC) tag was fused in frame with the C-terminus of TLAP2 gene (ToxoDb.org, TGGT1_232130) in the ΔKu80 strain using the ligation independent cloning strategy.[59] A 1.5 kb fragment corresponding to the 3′ end of the TLAP2 excluding the stop codon was amplified by PCR with the forward primer 5′-GCGCCCTCCTTCAGTGTTCTTC-3′ and reverse primer 5′-TGCACCCTGCGGCACCGGCAG-3′. The PCR fragment and vector p-LIC-mCherry-HXG were digested with T4 DNA polymerase and annealed, yielding plasmid pTLAP2mCherry-LIC-DHFR. Freshly egressed Δku80 tachyzoites from a 1/2 T25 flask were transfected with 15 μg of the EcoRV-linearized plasmid. After one cycle without drug, ΔKu80/TLAP2-mC transformants were selected with 2 μg/mL pyrimethamine and single-cell cloned by limiting dilution.

Endogenous tagging of MyoA with HA-tag was achieved using the pLIC-MyoA-HA-HXGPRT vector. To construct this plasmid the coding sequence of MyoA was amplified using primers 5′-TACTTCCAATCCAATTTAGCAAAGCAGCAAACTGCCCA-GCGAAG-3′ and 5′-TCCTCCACTTCCAATTTTAGC-GAACGCCGGCTGAACAGTCGCGGG-3′ and RH Δ*ku80* genomic DNA as template. The PCR product was cloned to pLIC-mAID-HA-HXGPRT vector using the LIC cloning method as described above.[61] RH*ku80* OsTir1-(Ty)3 parasites were electroporated with BstBI-linearized plasmid, and recombinant parasites were selected with mycophenolic acid (25 μg/mL) and xanthine (50 μg/mL). Stable transgenic parasites were single-cell cloned by limiting dilution.

Video Microscopy. Time-lapse video microscopy was conducted in Chamlide chambers (LCI Corp., Seoul, Korea) accommodating 18 mm diameter coverslips or 35 mm MatTek glass bottom dishes (Matek corporation) installed on an Eclipse Ti inverted confocal microscope (Nikon France Instruments, Champigny sur Marne, France) set up with a temperature and CO_2-controlled stage and chamber (LCI Corp., Seoul, Korea). The microscope was equipped with the sCMOS prime camera (Photometrics), a 60× objective, and a CSU X1 spinning disk (Yokogawa, Roper Scientific, Lisses, France). MetaMorph software was used for controlling the microscope (Universal Imaging Corporation, Roper Scientific, Lisses, France). All live microscopy was performed at 37 °C and 5% CO_2.

https://dx.doi.org/10.1021/acsnano.0c01893
ACS Nano XXXX, XXX, XXX−XXX

Image Processing. For image processing, we combined the use of ImageJ, Icy, MATLAB, ChimeraX, and Amira-Avizo (Thermo-Fisher) software. Details of image processing are included in the appropriate protocol sections. Slow motion videos were created using Adobe Premiere with the optical flow module.

Motility Assays in Collagen1 Fibrous Matrices. Collagen gels were made using rat tail type I collagen (CellSystems). Nine parts of collagen dissolved in acidic medium were mixed with 1 part of neutralization solution to reach the concentration of 4 mg/mL and promote matrix formation. All solutions were kept in 4 °C during preparation. Then dilution of the gel at a concentration of 2 mg/mL in $HBSS^{++}$ supplemented with 1% FCS was rapidly spread in the middle of a MatTek glass bottom dish and incubated for 30 min at 37 °C and 5% CO_2. Labeling of the collagen fibers was achieved with the recombinant CNA35-EGFP produced in *Escherichia coli* (BL21-DE3 strain) used at 2 μM final concentration according to the protocol.[35] A 50 μL volume of the tachyzoite suspension prepared in 1% FCS HBSS-Ca^{2+} was deposited on top of the gel prior to being transferred in the microscopy stage for video microscopy. Once tachyzoites had penetrated within the mesh, images were captured at 1 frame/s. For tracking the fibers during parasite navigation, we used Icy and visualized with green the initial position of the fibers at t = 0 s while we duplicated this frame as many times as the number of the time-lapse frames. Then we merged this "time zero" stack with the original time lapse in which the fibers were colored in magenta. The whitish color accounts for the green and magenta overlay and indicates no displacement, whereas the detection of the green and magenta reveals the fiber displacement during the sequence.

Tachyzoite 2D Gliding Assays. Parasites were prepared as described above, and assays were carried on 18 mm plasma-activated glass coverslips coated with either fibronectin (20−50 μg/mL in phosphate-buffered saline (PBS)) or poly-L-lysine (150−300 kDa PLL, 50 μg/mL in PBS). Image analysis included tracking the tachyzoite back and front parts over the gliding time by using Icy as described.[62] "Manual tracking" and "Motion profiler" plugins were used to extract the x−y position of the back and front spots over time. Having tracked the x−y positions over time, we used the "Distance profiler" plugin to calculate the distance between the two positions (back and front) over time.

Reflection Interference Contrast Microscopy. RICM images were acquired on an inverted microscope (IX71, Olympus) on which a white-light source (HPLS 345, Thorlabs) was coupled using a home-built illumination arm incorporating a diaphragm (SM1D12C, Thorlabs) controlling the illumination numerical aperture (NA = 0.46 in all experiments shown here) and a triple-band spectral filter (FF01-457/530/628-25, Semrock) as described.[63] The usual fluorescence cube in the microscope turret was replaced by polarization optics, allowing separation of the incoming and reflected light (polarizer WP25M-VIS, Thorlabs), polarizing beamsplitter cube (PBS251, Thorlabs), and achromatic imaging flat quarter waveplate (QWP; custom-made, Fichou, France). The sample was imaged with an oil-immersion objective (60XO UPLSApo, Olympus, Japan) onto a sCMOS camera (Orca Flash 4 v2, Hamamatsu) after passing through an autofocus device (CRISP system, ASI imaging, USA) and a home-built image-splitting setup incorporating a variable slit (VA100/M, Thorlabs), achromatic relay lenses (ITL200, Thorlabs), imaging flat dichroic mirrors (FF484-FDi01-25X36 and FF560-FDi01-25X36, Semrock) gently held through curable silicon paste (Sugru, Form-FormForm, UK), silver mirrors (PFSQ10-03-P01, Thorlabs) and dichroic filters (blue: Semrock FF01-452/45-25; green: FF01-531/46-25; red: FF01-629/56-25, Semrock). In addition, for bright-field (BF) imaging, a red colored glass filter (FGL610S, Thorlabs) was used to filter the light for the microscope illumination arm that was subsequently focused by a long-distance 0.3 NA condenser (all Olympus, Japan). BF and RICM images were acquired simultaneously, in the red channel, and thus show a dim RICM image superimposed. Finally, a custom-built thermostated box (Digital Pixel, UK) enclosing most of the microscope was used to control the temperature at the sample. Image processing was done using ImageJ. Blue, green, and red stacks of images were first manually registered. RICM images were subsequently filtered using the "FFT band-pass filter" plugin (1−100 pixels) to remove high-frequency noise and uneven illumination background. The two (in the case of simultaneous BF/RICM imaging) or three (in the case of only RICM imaging) RICM images were then superimposed and converted into a RGB image. BF images and RGB RICM images were then segmented using the "trainable Weka segmentation" plugin.[64] For BF images, the classifier was trained to segment the whole parasite, and the outline of the resulting binary image was extracted subsequently. For RICM images, the algorithm was used to separate the "close contact" area defined by the first dark RICM fringe on the parasite surface, the trail (when relevant), the rest of the RICM signal coming from the parasite (when no BF image was present), and the rest of the image. Because the classifier could detect the second dark RICM fringe manual correction of the segmented images was performed afterward to remove incorrect areas classified as "close contact". A binary image was obtained for the "close contact" area, whereas an 8-bit probability image was extracted for the trail. Analysis of the processed images was also performed using ImageJ. The kymograph was obtained using the plugin "KymoResliceWide". For measuring the speed of the parasite back end, the corresponding white line on the kymograph was isolated and the positions of the pixels were exported to Origin. After smoothing, the position curve was derived to obtain the velocity of the back end over time.

Traction Force Microscopy. TFM setting was adapted from ref 65. The 2 kPa PAA gels were made and mixed with TFM beads (FluoSpheres carboxylate-modified microspheres, ThermoFisher Scientific, 0.2 μm dark red fluorescent, λ: 660/680, 2% solid). The gel was top-coated with fibronectin (20 μg/mL, 30 min, 23 °C) diluted in sodium bicarbonate pH 8.3 (100 mM). Typical samples were made from stocks of 0.7 μL beads mixed in 165 μL of gel supplemented with 1 μL of both tetramethylethylenediamine (TEMED) and ammonium persulfate (APS) 10% using 20 μL of bead-gel suspension for an 18 mm diameter silanized glass coverslip. A 50 μL volume of the tachyzoite suspension prepared in 1% HBSS-Ca^{2+} (see above) was deposited on top of the fibronectin-coated PAA gel already filled with 100 μL of 1% HBSS-Ca^{2+} in the appropriate chamber and video recording started upon tachyzoite contact with the substrate. MetaMorph streaming option was used for fast recording (<1 frame/s) in both the DIC and far-red channels. Analysis of the TFM beads displacement for extracting the force values carried out using MATLAB. The TFM bead displacement was assessed using as a reference bead position, the frame with a gel area free of parasite (*i.e.*, relaxed position of the gel). Then using the frames taken over time, the bead's displacement was tracked from their initial relaxed position. To check the tachyzoite gliding behavior on a substrate of different stiffness, gels of different PAA concentration and coated with a layer of fibronectin were made using the same protocol, omitting the bead addition step, and the stiffness was controlled by atomic force microscopy.

Micropatterned Devices. Micropatterned PEG-fibronectin composite coverslips were engineered by Alveole using the PRIMO patterning with specific area coated with a mix of fibronectin (100 μg/mL) and AlexaFluor647-coupled fibrinogen (10 μg/mL) and other coated with PLL−PEG. Fifty microliters of the tachyzoite suspension prepared in 1% HBSS-Ca^{2+} was deposited on top of the fibronectin-coated glass coverslip placed in the chamber and prefilled with 100 μL of buffer prior to video microscopy.

Rear-Blocked Parasite Assay. The 0.2 μm diameter beads (FluoSpheres carboxylate-modified microspheres, ThermoFisher Scientific F8807, λ: 660/680, 2% solid) were activated using the microsphere coupling−two-step EDC/Sulfo NHS covalent coupling procedure for Estapor carboxyl-modified dyed microspheres protocol (MerckMillipore). Fifty microliters of the stock-activated bead solution was diluted in 150 μL of MES buffer (50 mM, pH 6.0). Then 30 μL of the bead solution was added to 120 μL of the tachyzoite suspension in 0.15% FCS $HBSS^{++}$ (0.15% HBSS). Fifty microliters of the parasite suspension (from either the RHΔKu80, ΔMyoA, RHΔKu80Acb-E, or YFP tachyzoite lines) was deposited on the (50 μg/mL) fibronectin-coated glass coverslips in the microscopy

https://dx.doi.org/10.1021/acsnano.0c01893
ACS Nano XXXX, XXX, XXX−XXX

chamber, which was already filled with 200 μL of 0.15% HBSS^{++}. In some experiments, parasites were preincubated for 10 min with 0.5 or 1 μM of either jasplakinolide or cytochalasin D (Sigma) and video-recorded in the presence of the compounds. For the intracellular mimicking conditions, tachyzoites collected by centrifugation in 0.15% HBSS^{++} were rinsed in ENDO buffer referred to here as IC buffer (145 mM KCl; 5 mM NaCl; 1 mM $MgCl_2$; 15 mM MES; 15 mM HEPES; pH 8.3)[66] before use, and the activated beads were prepared in IC buffer. The mixture prepared as mentioned above was deposited on the microscopy chamber, which was prefilled with 200 μL of IC buffer. Images were acquired at 1 s intervals for 20 min. To describe the contractile potential of tachyzoites under each experimental condition, we calculated the contraction ratio by measuring two times the length of the parasite body starting from the back until its farther apical point but excluding the conoid to avoid false measurements in case of fluctuating extrusion. The first measure corresponded to the relax position and the second to the maximal contraction. Division of the relaxed *versus* the contracted length provided the contraction ratio. When needed, both DIC and fluorescence channels were recorded at ~1 frame/s.

Bead Flow Assays. The assay was performed similarly to the rear blocked parasite assay. For tracking the beads, visualizing their tracks and extracting their speed, "Spot detector" and "Track manager" plugins (Icy) were used.

Expansion Microscopy. To analyze gliding tachyzoites, we collected the parasites in either in prewarmed 1% FCS HBSS-Ca^{2+} or IC buffer, which were centrifuged at low speed to synchronize their sedimentation and left to glide for 10 min on PLL (50 μg/mL)-coated plasma-activated glass coverslips (37 °C, 5% CO_2). Gliding was stopped by addition of paraformaldehyde (PFA, 3.2%, 15 min). The tachyzoite surface and trails were immunolabeled with anti-TgPSAG1 antibodies (mAb, clone TP3), and the chimeric TLAP2 protein was detected using the rabbit anti-mCherry antibodies (Institut Curie, TAb-IP Paris, France) directed against the mC tag after cell permeabilization with TritonX-100 (0.1% in PBS, 5 min). The samples were next incubated with appropriate secondary highly cross-adsorbed antibodies (4 μg/mL, 2h). The ExM protocol was adapted from ref 45. Briefly Acryloyl-X was used at 0.1 mg/mL PBS for 2 h at 23 °C prior to the gelation step, which was performed by placing the gelation solution (80 μL) on parafilm and the coverslip with the cell sample face down on top of it. Gelation was allowed to proceed at 37 °C for 1 h followed by the digestion step (0.5% Triton X-100, 8 units/mLProteinase K) carried out overnight at 23 °C. A 4 mm diameter gel core sample was collected with a puncher and immerged in 5 mL of ddH_2O in a 50 mm diameter Petri dish to promote expansion, while PI staining was concomitantly performed (2.5 μM in PBS). H_2O was exchanged every 20 min until maximal expansion. The piece of gel was next gently transferred onto a PLL-coated glass coverslip in the minimal liquid volume to avoid gel drift. The 0.2 μm *Z*-image stacks of parasites in stages were captured using a spinning disk confocal Eclipse-ti Nikon microscope.

Ultrastructure Expansion Microscopy. Gliding assays were performed with RHΔKu80MyoA-HA similarly to that for ExM. Additionally, for the invasion assay, HFF cells were plated on a poly-L-lysine-coated glass coverslip to obtain 80% cell confluence on the following day. Parasites were settled on top of the cells by gentle centrifugation (2 min, 250*g*) and left to invade for 1 h (37 °C, 5% CO_2). For U-ExM, we followed the protocol developed by the Guichard laboratory,[52] but to optimally preserve both free and intracellular tachyzoite shapes, we found it better to fix the samples before expansion in a solution made of 0.7% formaldehyde and 1% acrylamide in PBS (4−5 h, 37 °C). Next, similar to the ExM protocol, gelation was carried out for 1 h (37 °C). Coverslips with gels were then transferred into ~2 mL of the denaturation buffer in a 6-well plate for 15 min (23 °C). Gels were removed from the coverslips with tweezers and transferred to a 35 mm diameter glass Petri dish filled fresh denaturation buffer for a 60 min incubation at 95 °C. After denaturation, gels were placed in a 150 mm diameter glass Petri dish filled with ddH_2O for the first expansion. Water was exchanged at least twice every 30 min at room temperature, and gels were incubated overnight in ddH_2O. After limited shrinkage in PBS, several 4 mm diameter pieces of gel were collected and deposited on 24-well plates. Gels were then incubated for 3 h at 37 °C under shaking in primary antibodies (antiacetylated α-tubulin, mAb, clone 6-11B-1) or rabbit α- polyglutamylated (mAb, clone GT335) and rat anti-HA antibodies (mAb, clone 3F10). Gels were washed in PBS-Tween 0.1% prior to incubation with appropriate secondary highly cross-adsorbed antibodies (4 μg/mL) for 150 min at 37 °C and washed again in PBS-Tween 0.1%. Expansion was achieved by controlled immersion in ddH_2O. The PI staining, final ddH_2O wash, and gel mounting steps were all performed as mentioned for ExM.

ExM and U-ExM Image Processing. 3D reconstruction was achieved with the UCSF ChimeraX software from the raw data (*i.e.*, xyz files) processed with ImageJ to first crop the region of interest and then to apply the "Iterative Deconvolve 3D" plugin for each channel. We used the ImageJ "3D Object counter" plugin to check for the isotropic physical expansion of the specimen by comparing the ratio of the parasite (SAG1 staining) and the nucleus (PI staining) volumes in controlled and expanded extracellular tachyzoite samples. The nucleus sphericity index of motile, nonmotile, and intracellular tachyzoites was compared by thresholding each image object to create 3D binary images, whereas the "3D Object counter" plugin was next used to segment *Z*-stack binary images and retrieve the volume and surface of the 3D objects (*i.e.*, parasite nucleus and whole body). The sphericity index was calculated using the formula where V is the volume and S the surface:

$$\text{sphericity } \Psi = \frac{(36\pi V^2)^{1/3}}{S}$$

The nucleus roundness was obtained by thresholding a *Z*-Max projection from the *Z*-stack images and using the "Particle analysis" plugin.

For the tubulin curvature analysis in expanded specimens, we used the "Kappa" plugin in Fiji on the *Z*-Max projection from *Z*-stack images of the tachyzoite ventral cMTs (*i.e.*, facing the substrate), which allowed tracing each MT shape and retrieving the mean curvature of each cMT as well as the curvature amplitude over the cMT length (standard deviation).

MIC2 and SAG1 Analysis in Helical Trail. Extracellular tachyzoites were let to glide for 15 min prior to be fixed with PFA as described in the ExM section. A double immunolabeling was performed sequentially using the anti-TgSAG1 protein (clone TP3, 30 min, 23 °C) and the anti-TgMIC2 (clone 6D10, overnight, 4 °C) as primary antibodies, each followed by incubation with appropriate secondary highly cross-adsorbed antibodies (4 μg/mL, 2 h). Images were acquired on the Axio Imager Z1 Zeiss microscope using the Zeiss imaging software ZEN before being processed using Fiji software.

To determine the size and position of the adhesion point formed at the early step of the helical cycle (*i.e.*, coinciding with the kink) on the MIC2/SAG immunolabeled trails, we used the machine-learning-based segmentation of the real-time RICM sequence as a template. The region of interest for the trail trajectory, the angular area, and the parasite apical adhesion area were defined manually with Fiji: the distance between the center of adhesion point and the angle point was measured for six angles over a sequence of successive helical cycles, which allowed positioning the apical adhesion at about +0.170 μm downstream the angle point, and the size of the adhesion point was estimated around 0.5 μm. Applying these values on the MIC2/SAG1 labeled trails, it was possible to accurately identify the adhesion and angle area over the profiles of fluorescence intensity measured for the whole trails trajectories that in total defined 40 helical cycles performed by eight tachyzoites. The fluorescence intensity is given as a ratio by normalizing on the mean intensity value.

Quantification and Statistical Analysis. Data were statistically analyzed, and plots were made using GraphPad Prism 6.0 software for Windows (La Jolla, CA, USA). Data are presented as mean ± standard error of mean if not indicated otherwise. Figure legends include the statistical test and resulting comparison when appropriate.

https://dx.doi.org/10.1021/acsnano.0c01893
ACS Nano XXXX, XXX, XXX−XXX

For Figure 4A, Figure 7A, and Figures S3A and S5B,C, an unpaired *t* test was used with significance being represented as a *p* value <0.05, and the *n* indicated represents the parasite sample size or the number of individual microtubules analyzed. For Figure 4E, Figure 5A, and Figure S5A, an unpaired Kruskal–Wallis test was performed, and the *n* indicates the sample size. For the table in Figure 5A, a chi-square test followed by Fisher's exact text was used, with the *n* showing the proportions analyzed.

ASSOCIATED CONTENT

Supporting Information

The Supporting Information is available free of charge at https://pubs.acs.org/doi/10.1021/acsnano.0c01893.

Helical and circular gliding by *T. gondii* tachyzoites; tachyzoite apical adhesion site is not enriched in MIC2 and SAG1 proteins; frequency and duration of *T. gondii* tachyzoite gliding behavior depends on the substrate stiffness; prolonged and exacerbated contraction induced upon tachyzoite posterior immobilization leads to membrane leakage; expansion microscopy allows uncovering cMT local selective compression and torsion in gliding tachyzoites (PDF)

Movie 1: Parasite moving in 3D collagen fibers1 (AVI)

Movie 2: Parasite moving 3D collagen fibers2 (AVI)

Movie 3a: Parasite helical gliding in 2D (AVI)

Movie 3b: Slow motion but same as movie 3a (AVI)

Movie 4: Parasite circular gliding in 2D (AVI)

Movie 5: RICM analysis of parasite helical gliding (AVI)

Movie 6: RICM-pulling on or breaking the trail (AVI)

Movie 7a: TFM analysis of parasite helical gliding (AVI)

Movie 7b: Slow motion but same as movie 7a (AVI)

Movie 8: Parasite helical gliding on micropattern Alveole1 (AVI)

Movie 9: Parasite helical gliding micropattern Alveole2 (AVI)

Movie 10: Parasite base blocked by microbeads (AVI)

Movie 11: Bead release from the base of a moving parasite (AVI)

Movie 12: Parasite contraction in the presence of drugs (AVI)

Movie 13: Actin dynamics in gliding or immobilized parasites (AVI)

Movie 14: Bead flow and bead release in tachyzoites (AVI)

AUTHOR INFORMATION

Corresponding Author

Isabelle Tardieux − *Institute for Advanced Biosciences (IAB), Team Membrane Dynamics of Parasite−Host Cell Interactions, CNRS UMR5309, INSERM U1209, Université Grenoble Alpes, 38700 Grenoble, France;* orcid.org/0000-0002-5677-7463; Email: isabelle.tardieux@inserm.fr

Authors

Georgios Pavlou − *Institute for Advanced Biosciences (IAB), Team Membrane Dynamics of Parasite−Host Cell Interactions, CNRS UMR5309, INSERM U1209, Université Grenoble Alpes, 38700 Grenoble, France*

Bastien Touquet − *Institute for Advanced Biosciences (IAB), Team Membrane Dynamics of Parasite−Host Cell Interactions, CNRS UMR5309, INSERM U1209, Université Grenoble Alpes, 38700 Grenoble, France*

Luis Vigetti − *Institute for Advanced Biosciences (IAB), Team Membrane Dynamics of Parasite−Host Cell Interactions, CNRS UMR5309, INSERM U1209, Université Grenoble Alpes, 38700 Grenoble, France*

Patricia Renesto − *Institute for Advanced Biosciences (IAB), Team Membrane Dynamics of Parasite−Host Cell Interactions, CNRS UMR5309, INSERM U1209, Université Grenoble Alpes, 38700 Grenoble, France; TIMC-IMAG UMR 5525 - UGA CNRS, 38700 Grenoble, France*

Alexandre Bougdour − *Institute for Advanced Biosciences (IAB), Team Host−Pathogen Interactions & Immunity to Infections, CNRS UMR5309, INSERM U1209, Université Grenoble Alpes, 38700 Grenoble, France*

Delphine Debarre − *Laboratoire Interdisciplinaire de Physique, UMR CNRS, 5588, Université Grenoble Alpes, Grenoble 38402, France*

Martial Balland − *Laboratoire Interdisciplinaire de Physique, UMR CNRS, 5588, Université Grenoble Alpes, Grenoble 38402, France*

Complete contact information is available at: https://pubs.acs.org/10.1021/acsnano.0c01893

Author Contributions

Conceptualization, I.T., M.B, G.P; Software, M.B., D.D, G.P.; Formal Analysis, G.P., B.T., D.D, L.V.; Funding acquisition, I.T.; Investigation; G.P., B.T., I.T., V.L., D.D., P.R., A.B.; Methodology, I.T., G.P., B.T., A.B.; Project administration, I.T.; Supervision, I.T., M.B., P.R.; Validation, I.T., G.P., M.B., D.D.; Visualization, G.P., B.T., L.V.; Writing−original draft, I.T. Writing−review and editing, I.T., G.P., P.R., A.B., M.B., D.D.

Funding

This work has been funded by the IAB department "Prevention and Therapy of Chronic Diseases (Grenoble, France) with an internal grant. The University Grenoble-Alpes and the Fondation pour la Recherche Médicale (FRM FDT201904008408) awarded to G.P. with a 3 year Ph.D. fellowship and 6 month Ph.D. extension fellowship, respectively.

Notes

The authors declare no competing financial interest.

ACKNOWLEDGMENTS

We thank T. Boudou for help with the collagen gels, T. Andersen, V. Petrolli, and A. Ruppel for help in setting and analyzing the TFM assays. They all belong to the Laboratoire Interdisciplinaire de Physique, UMR CNRS, 5588, Université Grenoble Alpes, France. We thank C. Guilluy for the AFM assays to probe gels, M. Bogeda for help in micropatterning (IAB, Grenoble), and the Alveole team for providing the composite micropatterns. We thank the therapeutic antibodies (Tab-IP) and recombinant antibodies platform from the Curie Institute, Paris, France for providing the anti-mCherry antibodies.

REFERENCES

(1) Scarpa, E.; Mayor, R. Collective Cell Migration in Development. *J. Cell Biol.* **2016**, *212*, 143−155.

(2) Friedl, P.; Weigelin, B. Interstitial Leukocyte Migration and Immune Function. *Nat. Immunol.* **2008**, *9*, 960−969.

(3) Tschumperlin, D. J. Fibroblasts and the Ground They Walk On. *Physiology* **2013**, *28*, 380−390.

(4) Raftopoulou, M.; Hall, A. Cell Migration: Rho GTPases Lead the Way. *Dev. Biol.* **2004**, *265*, 23−32.
(5) Gardel, M. L.; Schneider, I. C.; Aratyn-Schaus, Y.; Waterman, C. M. Mechanical Integration of Actin and Adhesion Dynamics in Cell Migration. *Annu. Rev. Cell Dev. Biol.* **2010**, *26*, 315−333.
(6) Yamada, K. M.; Sixt, M. Mechanisms of 3D Cell Migration. *Nat. Rev. Mol. Cell Biol.* **2019**, *20*, 738−752.
(7) Petrie, R. J.; Koo, H.; Yamada, K. M. Generation of Compartmentalized Pressure by a Nuclear Piston Governs Cell Motility in a 3D Matrix. *Science* **2014**, *345*, 1062−1065.
(8) Copos, C. A.; Walcott, S.; del Álamo, J. C.; Bastounis, E.; Mogilner, A.; Guy, R. D. Mechanosensitive Adhesion Explains Stepping Motility in Amoeboid Cells. *Biophys. J.* **2017**, *112*, 2672−2682.
(9) Robert-Gangneux, F.; Darde, M.-L. Epidemiology of and Diagnostic Strategies for Toxoplasmosis. *Clin. Microbiol. Rev.* **2012**, *25*, 264−296.
(10) Tardieux, I.; Baum, J. Reassessing the Mechanics of Parasite Motility and Host-Cell Invasion. *J. Cell Biol.* **2016**, *214*, 507−515.
(11) Håkansson, S.; Morisaki, H.; Heuser, J.; Sibley, L. D. Time-Lapse Video Microscopy of Gliding Motility in *Toxoplasma Gondii* Reveals a Novel, Biphasic Mechanism of Cell Locomotion. *Mol. Biol. Cell* **1999**, *10*, 3539−3547.
(12) Amino, R.; Thiberge, S.; Martin, B.; Celli, S.; Shorte, S.; Frischknecht, F.; Ménard, R. Quantitative Imaging of *Plasmodium* Transmission from Mosquito to Mammal. *Nat. Med.* **2006**, *12*, 220−224.
(13) Münter, S.; Sabass, B.; Selhuber-Unkel, C.; Kudryashev, M.; Hegge, S.; Engel, U.; Spatz, J. P.; Matuschewski, K.; Schwarz, U. S.; Frischknecht, F. *Plasmodium* Sporozoite Motility Is Modulated by the Turnover of Discrete Adhesion Sites. *Cell Host Microbe* **2009**, *6*, 551−562.
(14) Frischknecht, F.; Matuschewski, K. *Plasmodium* Sporozoite Biology. *Cold Spring Harbor Perspect. Med.* **2017**, *7*, a025478.
(15) Amino, R.; Giovannini, D.; Thiberge, S.; Gueirard, P.; Boisson, B.; Dubremetz, J.-F.; Prévost, M.-C.; Ishino, T.; Yuda, M.; Ménard, R. Host Cell Traversal Is Important for Progression of the Malaria Parasite through the Dermis to the Liver. *Cell Host Microbe* **2008**, *3*, 88−96.
(16) Kan, A.; Tan, Y.-H.; Angrisano, F.; Hanssen, E.; Rogers, K. L.; Whitehead, L.; Mollard, V. P.; Cozijnsen, A.; Delves, M. J.; Crawford, S.; Sinden, R. E.; McFadden, G. I.; Leckie, C.; Bailey, J.; Baum, J. Quantitative Analysis of *Plasmodium* Ookinete Motion in Three Dimensions Suggests a Critical Role for Cell Shape in the Biomechanics of Malaria Parasite Gliding Motility. *Cell. Microbiol.* **2014**, *16*, 734−750.
(17) Bichet, M.; Joly, C.; Hadj Henni, A.; Guilbert, T.; Xemard, M.; Tafani, V.; Lagal, V.; Charras, G.; Tardieux, I. The *Toxoplasma*-Host Cell Junction Is Anchored to the Cell Cortex to Sustain Parasite Invasive Force. *BMC Biol.* **2014**, *12*, 773.
(18) Frixione, E.; Mondragón, R.; Meza, I. Kinematic Analysis of *Toxoplasma Gondii* Motility. *Cell Motil. Cytoskeleton* **1996**, *34*, 152−163.
(19) Leung, J. M.; Rould, M. A.; Konradt, C.; Hunter, C. A.; Ward, G. E. Disruption of TgPHIL1 Alters Specific Parameters of *Toxoplasma Gondii* Motility Measured in a Quantitative, Three-Dimensional Live Motility Assay. *PLoS One* **2014**, *9*, No. e85763.
(20) Carruthers, V. B.; Tomley, F. M. Receptor-Ligand Interaction and Invasion: Microneme Proteins in Apicomplexans. *Subcell Biochem* **2008**, *47*, 33−45.
(21) Lagal, V.; Binder, E. M.; Huynh, M.-H.; Kafsack, B. F. C.; Harris, P. K.; Diez, R.; Chen, D.; Cole, R. N.; Carruthers, V. B.; Kim, K. *Toxoplasma Gondii* Protease TgSUB1 Is Required for Cell Surface Processing of Micronemal Adhesive Complexes and Efficient Adhesion of Tachyzoites: TgSUB1Microneme Protein Processing. *Cell. Microbiol.* **2010**, *12*, 1792−1808.
(22) Opitz, C.; Soldati, D. The Glideosome: A Dynamic Complex Powering Gliding Motion and Host Cell Invasion by *Toxoplasma Gondii*. *Mol. Microbiol.* **2002**, *45*, 597−604.
(23) Frénal, K.; Dubremetz, J.-F.; Lebrun, M.; Soldati-Favre, D. Gliding Motility Powers Invasion and Egress in Apicomplexa. *Nat. Rev. Microbiol.* **2017**, *15*, 645−660.
(24) Andenmatten, N.; Egarter, S.; Jackson, A. J.; Jullien, N.; Herman, J.-P.; Meissner, M. Conditional Genome Engineering in *Toxoplasma Gondii* Uncovers Alternative Invasion Mechanisms. *Nat. Methods* **2013**, *10*, 125−127.
(25) Bichet, M.; Touquet, B.; Gonzalez, V.; Florent, I.; Meissner, M.; Tardieux, I. Genetic Impairment of Parasite Myosin Motors Uncovers the Contribution of Host Cell Membrane Dynamics to *Toxoplasma* Invasion Forces. *BMC Biol.* **2016**, *14*, 97.
(26) Graindorge, A.; Frénal, K.; Jacot, D.; Salamun, J.; Marq, J. B.; Soldati-Favre, D. The Conoid Associated Motor MyoH Is Indispensable for *Toxoplasma Gondii* Entry and Exit from Host Cells. *PLoS Pathog.* **2016**, *12*, No. e1005388.
(27) Morrissette, N. S.; Sibley, L. D. Cytoskeleton of Apicomplexan Parasites. *Microbiol. Mol. Biol. Rev.* **2002**, *66*, 21−38.
(28) Frénal, K.; Polonais, V.; Marq, J.-B.; Stratmann, R.; Limenitakis, J.; Soldati-Favre, D. Functional Dissection of the Apicomplexan Glideosome Molecular Architecture. *Cell Host Microbe* **2010**, *8*, 343−357.
(29) Mueller, C.; Graindorge, A.; Soldati-Favre, D. Functions of Myosin Motors Tailored for Parasitism. *Curr. Opin. Microbiol.* **2017**, *40*, 113−122.
(30) Liu, J.; He, Y.; Benmerzouga, I.; Sullivan, W. J.; Morrissette, N. S.; Murray, J. M.; Hu, K. An Ensemble of Specifically Targeted Proteins Stabilizes Cortical Microtubules in the Human Parasite *Toxoplasma Gondii*. *Mol. Biol. Cell* **2016**, *27*, 549−571.
(31) Quadt, K. A.; Streichfuss, M.; Moreau, C. A.; Spatz, J. P.; Frischknecht, F. Coupling of Retrograde Flow to Force Production During Malaria Parasite Migration. *ACS Nano* **2016**, *10*, 2091−2102.
(32) Whitelaw, J. A.; Latorre-Barragan, F.; Gras, S.; Pall, G. S.; Leung, J. M.; Heaslip, A.; Egarter, S.; Andenmatten, N.; Nelson, S. R.; Warshaw, D. M.; Ward, G. E.; Meissner, M. Surface Attachment, Promoted by the Actomyosin System of *Toxoplasma Gondii* Is Important for Efficient Gliding Motility and Invasion. *BMC Biol.* **2017**, *15*, 1.
(33) Tosetti, N.; Dos Santos Pacheco, N.; Soldati-Favre, D.; Jacot, D. Three F-Actin Assembly Centers Regulate Organelle Inheritance, Cell-Cell Communication and Motility in *Toxoplasma gondii*. *eLife* **2019**, *8*, e42669.
(34) Mouw, J. K.; Ou, G.; Weaver, V. M. Extracellular Matrix Assembly: A Multiscale Deconstruction. *Nat. Rev. Mol. Cell Biol.* **2014**, *15*, 771−785.
(35) Aper, S. J. A.; van Spreeuwel, A. C. C.; van Turnhout, M. C.; van der Linden, A. J.; Pieters, P. A.; van der Zon, N. L. L.; de la Rambelje, S. L.; Bouten, C. V. C.; Merkx, M. Colorful Protein-Based Fluorescent Probes for Collagen Imaging. *PLoS One* **2014**, *9*, No. e114983.
(36) Ejigiri, I.; Ragheb, D. R. T.; Pino, P.; Coppi, A.; Bennett, B. L.; Soldati-Favre, D.; Sinnis, P. Shedding of TRAP by a Rhomboid Protease from the Malaria Sporozoite Surface Is Essential for Gliding Motility and Sporozoite Infectivity. *PLoS Pathog.* **2012**, *8*, No. e1002725.
(37) Huynh, M.-H.; Carruthers, V. B. *Toxoplasma* MIC2 Is a Major Determinant of Invasion and Virulence. *PLoS Pathog.* **2006**, *2*, No. e84.
(38) Gras, S.; Jackson, A.; Woods, S.; Pall, G.; Whitelaw, J.; Leung, J. M.; Ward, G. E.; Roberts, C. W.; Meissner, M. Parasites Lacking the Micronemal Protein MIC2 Are Deficient in Surface Attachment and Host Cell Egress, but Remain Virulent *In Vivo*. *Wellcome Open Res.* **2017**, *2*, 32.
(39) Buguliskis, J. S.; Brossier, F.; Shuman, J.; Sibley, L. D. Rhomboid 4 (ROM4) Affects the Processing of Surface Adhesins and Facilitates Host Cell Invasion by *Toxoplasma Gondii*. *PLoS Pathog.* **2010**, *6*, No. e1000858.
(40) Martiel, J.-L.; Leal, A.; Kurzawa, L.; Balland, M.; Wang, I.; Vignaud, T.; Tseng, Q.; Théry, M. Measurement of Cell Traction Forces with ImageJ. *Methods Cell Biol.* **2015**, *125*, 269−287.

https://dx.doi.org/10.1021/acsnano.0c01893
ACS Nano XXXX, XXX, XXX−XXX

(41) Hegge, S.; Uhrig, K.; Streichfuss, M.; Kynast-Wolf, G.; Matuschewski, K.; Spatz, J. P.; Frischknecht, F. Direct Manipulation of Malaria Parasites with Optical Tweezers Reveals Distinct Functions of *Plasmodium* Surface Proteins. *ACS Nano* **2012**, *6*, 4648−4662.
(42) Stadler, R. V.; White, L. A.; Hu, K.; Helmke, B. P.; Guilford, W. H. Direct Measurement of Cortical Force Generation and Polarization in a Living Parasite. *Mol. Biol. Cell* **2017**, *28*, 1912−1923.
(43) Biais, N.; Higashi, D. L.; Brujic, J.; So, M.; Sheetz, M. P. Force-Dependent Polymorphism in Type IV Pili Reveals Hidden Epitopes. *Proc. Natl. Acad. Sci. U. S. A.* **2010**, *107*, 11358−11363.
(44) Perschmann, N.; Hellmann, J. K.; Frischknecht, F.; Spatz, J. P. Induction of Malaria Parasite Migration by Synthetically Tunable Microenvironments. *Nano Lett.* **2011**, *11*, 4468−4474.
(45) Asano, S. M.; Gao, R.; Wassie, A. T.; Tillberg, P. W.; Chen, F.; Boyden, E. S. Expansion Microscopy: Protocols for Imaging Proteins and RNA in Cells and Tissues. *Curr. Protoc. Cell Biol.* **2018**, *80*, No. e56.
(46) Egarter, S.; Andenmatten, N.; Jackson, A. J.; Whitelaw, J. A.; Pall, G.; Black, J. A.; Ferguson, D. J. P.; Tardieux, I.; Mogilner, A.; Meissner, M. The *Toxoplasma* Acto-MyoA Motor Complex Is Important but Not Essential for Gliding Motility and Host Cell Invasion. *PLoS One* **2014**, *9*, No. e91819.
(47) Bubb, M. R.; Spector, I.; Beyer, B. B.; Fosen, K. M. Effects of Jasplakinolide on the Kinetics of Actin Polymerization. An Explanation for Certain *In Vivo* Observations. *J. Biol. Chem.* **2000**, *275*, 5163−5170.
(48) Sampath, P.; Pollard, T. D. Effects of Cytochalasin, Phalloidin, and PH on the Elongation of Actin Filaments. *Biochemistry* **1991**, *30*, 1973−1980.
(49) Periz, J.; Whitelaw, J.; Harding, C.; Gras, S.; Del Rosario Minina, M. I.; Latorre-Barragan, F.; Lemgruber, L.; Reimer, M. A.; Insall, R.; Heaslip, A.; Meissner, M. *Toxoplasma Gondii* F-Actin Forms an Extensive Filamentous Network Required for Material Exchange and Parasite Maturation. *eLife* **2017**, *6*, e24119.
(50) Shaw, M. K.; Tilney, L. G. Induction of an Acrosomal Process in *Toxoplasma Gondii*: Visualization of Actin Filaments in a Protozoan Parasite. *Proc. Natl. Acad. Sci. U. S. A.* **1999**, *96*, 9095−9099.
(51) Del Rosario, M.; Periz, J.; Pavlou, G.; Lyth, O.; Latorre-Barragan, F.; Das, S.; Pall, G. S.; Stortz, J. F.; Lemgruber, L.; Whitelaw, J. A.; Baum, J.; Tardieux, I.; Meissner, M. Apicomplexan F-Actin Is Required for Efficient Nuclear Entry during Host Cell Invasion. *EMBO Rep.* **2019**, *20*, e48896.
(52) Gambarotto, D.; Zwettler, F. U.; Le Guennec, M.; Schmidt-Cernohorska, M.; Fortun, D.; Borgers, S.; Heine, J.; Schloetel, J.-G.; Reuss, M.; Unser, M.; Boyden, E. S.; Sauer, M.; Hamel, V.; Guichard, P. Imaging Cellular Ultrastructures Using Expansion Microscopy (U-ExM). *Nat. Methods* **2019**, *16*, 71−74.
(53) Plessmann, U.; Reiter-Owona, I.; Lechtreck, K.-F. Posttranslational Modifications of α-Tubulin of *Toxoplasma Gondii*. *Parasitol. Res.* **2004**, *94*, 386−389.
(54) Brangwynne, C. P.; MacKintosh, F. C.; Kumar, S.; Geisse, N. A.; Talbot, J.; Mahadevan, L.; Parker, K. K.; Ingber, D. E.; Weitz, D. A. Microtubules Can. Bear Enhanced Compressive Loads in Living Cells Because of Lateral Reinforcement. *J. Cell Biol.* **2006**, *173*, 733−741.
(55) Kabir, A. Md. R.; Inoue, D.; Afrin, T.; Mayama, H.; Sada, K.; Kakugo, A. Buckling of Microtubules on a 2D Elastic Medium. *Sci. Rep.* **2015**, *5*, 17222.
(56) Leung, J. M.; He, Y.; Zhang, F.; Hwang, Y.-C.; Nagayasu, E.; Liu, J.; Murray, J. M.; Hu, K. Stability and Function of a Putative Microtubule-Organizing Center in the Human Parasite *Toxoplasma Gondii*. *Mol. Biol. Cell* **2017**, *28*, 1361−1378.
(57) Harding, C. R.; Gow, M.; Kang, J. H.; Shortt, E.; Manalis, S. R.; Meissner, M.; Lourido, S. Alveolar Proteins Stabilize Cortical Microtubules in *Toxoplasma Gondii*. *Nat. Commun.* **2019**, *10*, 401.
(58) Cramer, L. P. Forming the Cell Rear First: Breaking Cell Symmetry to Trigger Directed Cell Migration. *Nat. Cell Biol.* **2010**, *12*, 628−632.
(59) Huynh, M.-H.; Carruthers, V. B. Tagging of Endogenous Genes in a *Toxoplasma Gondii* Strain Lacking Ku80. *Eukaryotic Cell* **2009**, *8*, 530−539.
(60) Andenmatten, N.; Egarter, S.; Jackson, A. J.; Jullien, N.; Herman, J.-P.; Meissner, M. Conditional Genome Engineering in *Toxoplasma Gondii* Uncovers Alternative Invasion Mechanisms. *Nat. Methods* **2013**, *10*, 125−127.
(61) Farhat, D. C.; Swale, C.; Dard, C.; Cannella, D.; Ortet, P.; Barakat, M.; Sindikubwabo, F.; Belmudes, L.; De Bock, P.-J.; Couté, Y.; Bougdour, A.; Hakimi, M.-A. A MORC-Driven Transcriptional Switch Controls *Toxoplasma* Developmental Trajectories and Sexual Commitment. *Nat. Microbiol.* **2020**, *5*, 570−583.
(62) Pavlou, G.; Tardieux, I. Phenotyping *Toxoplasma* Invasive Skills by Fast Live Cell Imaging. *Methods Mol. Biol.* **2020**, *2071*, 209−220.
(63) Davies, H. S.; Baranova, N. S.; El Amri, N.; Coche-Guérente, L.; Verdier, C.; Bureau, L.; Richter, R. P.; Débarre, D. An Integrated Assay to Probe Endothelial Glycocalyx-Blood Cell Interactions under Flow in Mechanically and Biochemically Well-Defined Environments. *Matrix Biol.* **2019**, *78*−*79*, 47−59.
(64) Arganda-Carreras, I.; Kaynig, V.; Rueden, C.; Eliceiri, K. W.; Schindelin, J.; Cardona, A.; Sebastian Seung, H. Trainable Weka Segmentation: A Machine Learning Tool for Microscopy Pixel Classification. *Bioinformatics* **2017**, *33*, 2424−2426.
(65) Martiel, J.-L.; Leal, A.; Kurzawa, L.; Balland, M.; Wang, I.; Vignaud, T.; Tseng, Q.; Théry, M. Measurement of Cell Traction Forces with ImageJ. *Methods Cell Biol.* **2015**, *125*, 269−287.
(66) Moudy, R.; Manning, T. J.; Beckers, C. J. The Loss of Cytoplasmic Potassium upon Host Cell Breakdown Triggers Egress of *Toxoplasma Gondii*. *J. Biol. Chem.* **2001**, *276*, 41492−41501.

https://dx.doi.org/10.1021/acsnano.0c01893
ACS Nano XXXX, XXX, XXX−XXX